SAND2026-15653J

The Effects of Shockwave Pressures on Ultrafast Vibrational Energy Transfer in BNFF, a Hydrogen-Free Energetic Material

Daniel Carlson,[†] River Leversee,[‡] Paul Schrader,[†] Kendrew Au,[†] Robert Knepper,[¶] Mitchell Wood,[*,§] and Krupa Ramasesha[*,†]

[†]*Combustion Research Facility, Sandia National Laboratories, Livermore, California 94550, United States*

[‡]*University of Colorado, Boulder, Colorado 80309, United States*

[¶]*Explosive Technologies Group, Sandia National Laboratories, Albuquerque, New Mexico 87185, United States*

[§]*Center for Computing Research, Sandia National Laboratories, Albuquerque, New Mexico 87185, United States*

E-mail: mitwood@sandia.gov; kramase@sandia.gov

Abstract

Energy conversion in energetic materials from shockwave-induced lattice compression to bond breaking critically depends on vibrational coupling and energy transfer between intra- and intermolecular vibrations, though the details of the mechanisms remain unknown. Herein, we indirectly tune the strength of intermolecular interactions in 3,4-bis(3-nitrofurazan-4-yl)furoxan (BNFF), a hydrogen-free energetic material characterized by van der Waals interactions, by applying high static pressure using a diamond anvil cell and monitoring vibrational energy transfer (VET) with ultrafast broadband infrared pump-probe spectroscopy. As BNFF is compressed from ambient pressure to 9 GPa, we find VET accelerates by ∼0.9 ps/GPa. Density functional theory is applied in tandem with experiment to assign mode character and elucidate VET pathways. We find that furazan ring O-N-O vibrations, which are high-frequency detonation-relevant vibrational modes, experience increased sensitivity to lattice compression under shockwave pressures. These findings provide new mechanistic insight into how intermolecular interactions govern the rate and selectivity of VET.

TOC Graphic

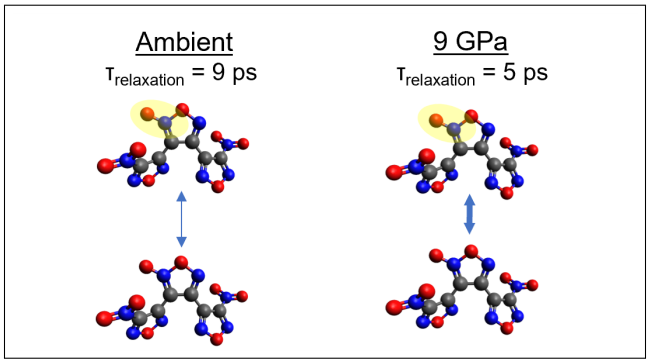

Keywords

Vibrational Energy Transfer, bis(nitrofurazano)furazan, BNFF, DNTF, Energetic Materials, Ultrafast Spectroscopy, Broadband Infrared, Transient Absorption Spectroscopy, Diamond

Anvil Cell, High Pressure

Understanding the complex mechanisms underlying the shock-to-detonation transition in energetic materials (EMs) is critical for future targeted designs to improve performance and safety in tandem.[1,2] The shock-to-detonation transition spans multiple orders of magnitude in time and is intricately linked to both molecular properties and microstructure of the material, posing significant challenges to the development of predictive models that can capture the fundamental chemical mechanisms. A central question is how delocalized lattice compression via shockwave excitation drives energy into intramolecular vibrational modes to then break chemical bonds. One hypothesized mechanism of energy transfer is the multiphonon up-pumping model,[3,4] which posits that a high population of low-frequency phonon modes behind a shock wave scatter into distinct doorway modes that bridge phonon vibrations and intramolecular vibrations, enabling a ladder-climbing process and eventually exciting multiple quanta in high-frequency vibrations. This has become a prominent model due to the strong correlations found between impact sensitivity and vibrational properties.[5,6] These models, however, often necessitate a somewhat arbitrary demarcation between intra- and intermolecular vibrational modes, typically defined by a frequency cutoff ω_{max}. Consequently, the precise time-dependent pathways of vibrational energy transfer (VET) and the quantitative contributions of intra- and intermolecular coupling remain open questions.[7–10]

Prior investigations of VET in EMs include Raman spectroscopy with picosecond time resolution of solvated energetics and monolayers[11,12] and two-dimensional infrared spectroscopy of a small subset of vibrational modes in solid EMs[13,14] as well as both solvated and suspended structural forms.[15] Shock-initiated VET and chemistry studies have been successful in mimicking real-world environments;[16–19] however, detailed insight into fundamental VET mechanisms is obscured by other important factors, such as defect-induced hot-spot formation. To study core aspects of VET in an unambiguous manner, our work simultaneously probes a wide range of IR-active vibrational modes of thin-film EMs via ultrafast broadband infrared transient absorption spectroscopy after a tunable narrowband IR pump excitation.[20] In pentaerythritol tetranitrate (PETN)[21] and 1,3,5-trinitroperhydro-

1,3,5-triazine (RDX),[22] VET was found to exist in three distinct sequential regimes: anharmonic coupling apparent within the instrument response function (∼250 fs), followed by an $\mathcal{O}$(1 ps) to $\mathcal{O}$(10 ps) vibrational energy relaxation, and lastly, a much slower $\mathcal{O}$(100 ps) time constant that was speculated to arise from a non-equilibrated phonon bath influencing select high-frequency vibrations. This $\mathcal{O}$(100 ps) lifetime revealed that VET is incomplete out to the 300 ps measurement range of the experiments, a stark contradiction to the multi-phonon up-pumping model where VET is predicted to be complete within tens of picoseconds.[3] In RDX in particular, this $\mathcal{O}$(100 ps) time-constant was found to be mode-specific, indicating that select high-frequency intramolecular vibrations were directly coupled to lattice vibrations.[23,24] Ongoing VET at these extended timescales would suggest initial shock-induced decomposition reactions would occur when thermal equilibrium has yet to be achieved.[25] In addition to the potential non-statistical nature of VET-mediated reactions, the direct connection between lattice and intramolecular modes would necessitate adaptation of the multiphonon up-pumping model.

To explore the effect of intermolecular interaction strength on VET dynamics in a somewhat controlled manner, this work applies broadband infrared pump-probe spectroscopy in tandem with density functional theory (DFT) to study bis(nitrofurazano)furazan (BNFF)—a hydrogen-free energetic material that is characterized by weak van der Waals interactions—subjected to static pressures in a diamond anvil cell (DAC). Applying a static tunable pressure to the material allows for an unambiguous pathway towards determining the effect of pressure on the VET dynamics. Additionally, this material is unlike previously studied hydrogen-containing EMs, which are characterized by stronger, hydrogen-bonding interactions. To date, no experimental VET studies have been performed on hydrogen-free EMs, while recent theoretical studies on BNFF[14,26] highlight renewed interest in this class of material due to its unique molecular crystal environment. By employing variable static pressure on a van der Waals bonded material, we can indirectly tune the intermolecular interaction strength in a continuous manner without introducing the complexity of phase transitions or

rearrangement effects often observed in hydrogen-bonded materials.

Figure 1 depicts the experimental infrared absorption spectrum of BNFF from ambient pressure to 9 GPa, and the corresponding DFT one-phonon density of states (DoS) are charted alongside the experimental data. From these calculations, we are able to assign mode character as shown in the lower right and upper right of Figure 1. As static pressure is applied to BNFF within the DAC, all vibrational modes shift to higher frequencies and broaden in linewidth. For example, the 1286 cm^{-1} mode (assigned as N-O symmetric stretch and C-C-C bending) at ambient pressure shifts to 1317 cm^{-1} at 9 GPa, and the 1001 cm^{-1} mode (N-O-N bending + C-backbone deformation) at ambient pressure shifts to 1015 cm^{-1} at 9 GPa. Some overlapping vibrational modes at ambient pressures become well-separated peaks at higher pressures, as seen for example, in the ambient pressure modes at 825 cm^{-1} (ring NO asymmetric stretch + NO_2 bending) and 1043 cm^{-1} (ring O-N-O symmetric stretch). Conversely, the 1523 cm^{-1} (amine N-O asymmetric stretch) and 1274 cm^{-1} modes appear to merge with neighbors under pressure. The 881 cm^{-1} and 1412 cm^{-1} modes disappear completely above 4.5 GPa. Detailed DFT mode assignments are presented in the SI (section S2.1). These results are consistent with a previous study of BNFF's pressure-dependent IR absorption.[27]

The narrowband IR pump pulse in our experiment is centered on the furoxan N-O asymmetric stretch vibration at 1642 cm^{-1}. The probe pulse spans most of the IR-active BNFF vibrational modes in the mid-IR, from $\sim$800 cm^{-1} to 1650 cm^{-1}, allowing our experiment to capture global VET pathways. The time-resolved BNFF absorption spectra following pump excitation for several spectral windows versus static pressure are presented in Figure 2, with additional results located in the SI (section S3). For each absorption feature in the FTIR spectrum, there is a corresponding doublet feature in the transient absorption spectrum due to the interaction of the probe pulse with a pump-excited sample: an induced transparency or bleach feature (negative, blue) due to stimulated emission by the probe and the loss of ground state absorption upon excitation, and an anharmonically shifted induced

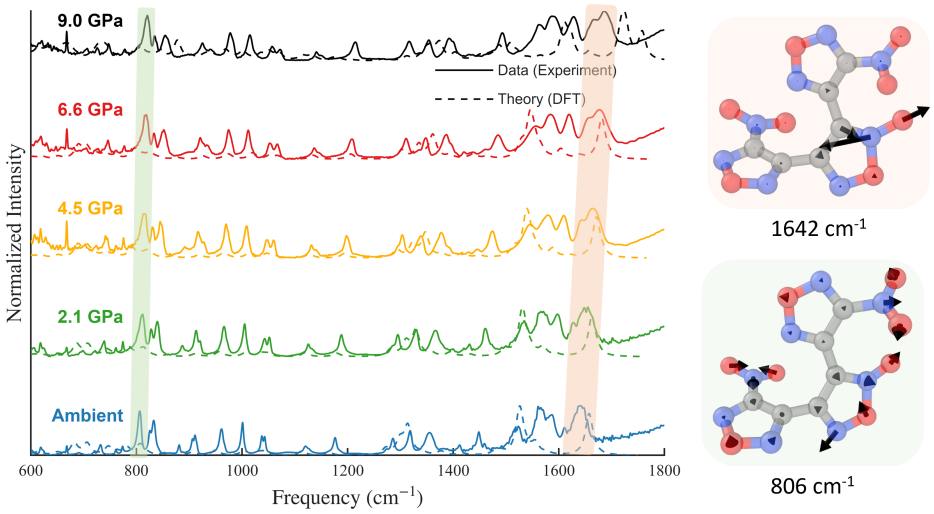

Figure 1: (Left) FTIR Absorption Spectra of BNFF vs pressure, overlaid with DFT one-phonon DoS results. (Top Right) The DFT mode assignment calculated for the pumped 1642 cm^{-1} mode, showing furoxan N-O asymmetric stretch character. (Lower Right) The DFT mode assignment calculated for the 806 cm^{-1} mode, showing NO_2 symmetric stretch + NONO dihedral bend character.

absorption feature (positive, red) due to further absorption of the probe pulse to yield a v=1 $\rightarrow$ 2 transition. In most cases, as discussed in previous ultrafast IR VET studies,[22] these doublet lineshapes, which are hallmarks of vibrational excitation, can be distinguished from a thermally-shifted v=0 $\rightarrow$ 1 ground state spectrum, as the latter is accompanied by dynamically broadening linewidths and a redshift of the transition.

Global analysis of the transient IR spectra was performed with a 4-lifetime sequential kinetic model to extract global time constants (see SI, section S4); the results are shown in Table 1. The instrument response function (IRF) is found to be $<$ 400 fs (see SI, section S1.2). Due to strong scattering of the pump pulse, spectral windows capturing the pump frequency were omitted in the fitting analysis. Across all pressures, we recover the same lifetime regimes found in previous VET studies of hydrogen-containing energetic materials, further confirming these time scale regimes as largely material-independent: (i) anharmonic coupling between the pumped mode and all probed IR-active vibrational modes manifested as a broad-spectrum response within the IRF, (ii) a global $\mathcal{O}$(1 ps) vibrational relaxation to what appears to be a thermally-shifted ground state, i.e., the difference between low and

high temperature IR spectra, characterized by positive absorption on the high frequency side of the bleach due to spectral broadening and redshifting at higher temperature, and (iii) a final $\mathcal{O}$(100 ps) time constant from the continued evolution of low-frequency vibrations. We find that the lineshape changes accompanying the $\mathcal{O}$(1 ps) lifetime is subdued in BNFF compared to PETN and RDX, which is a direct consequence of weaker van der Waals intermolecular interactions in BNFF yielding less pronounced broadening/shifting during vibrational relaxation of the high frequency modes. The $\mathcal{O}$(100 ps) lifetime is found to be mode-specific, similar to RDX.[22] By comparing the adjusted-R^2 values of the global fit with and without the $\mathcal{O}$(100 ps) lifetime included (see section S5.1 in SI), mode participation in this long time scale evolution can be established, where strong participation corresponds to the greatest improvement in adjusted-R^2. This analysis reveals that there is no straightforward binary assignment for which modes participate and which do not. Even upon inspecting the extremes of the analysis, no strong common structural motifs are found, consistent with previous VET studies.[22] Strong participation in the $\mathcal{O}$(100 ps) dynamics was found, for example, in the 1449 cm^{-1} (C-N stretch on the backbone), 1319 cm^{-1} (NO_2 symmetric stretch + C-N furazan stretch), and 1120 cm^{-1} (C-C-N angle bend + N-O-N furoxan angle bend) modes. On the other hand, minimal $\mathcal{O}$(100 ps) participation was found, for example, in the 911 cm^{-1} (in-plane furazan ring breathing), 1038 cm^{-1} (O-N-O angle on furazan ring), 806 cm^{-1} (NO_2 symmetric stretch + NONO dihedral angle bending), and 1042 cm^{-1} (O-N-O symmetric stretch on furazan ring) modes.

As pressure is applied in the diamond anvil cell, unsurprisingly, the bleach and induced absorption features shift to higher frequencies and broaden as seen by comparing the columns in Figure 2, consistent with the trends observed in the static infrared spectra (Figure 1). There is also a time-dependent shift in the central frequency of both bleach and induced absorption features. For example, in the bleach around 1079 cm^{-1} at 9 GPa, there is a clear $\mathcal{O}$(1 ps) evolution as the center frequency drifts lower, then there is an $\mathcal{O}$(100 ps) drift back to higher frequencies, accompanied by slight broadening. The spectral lineshape

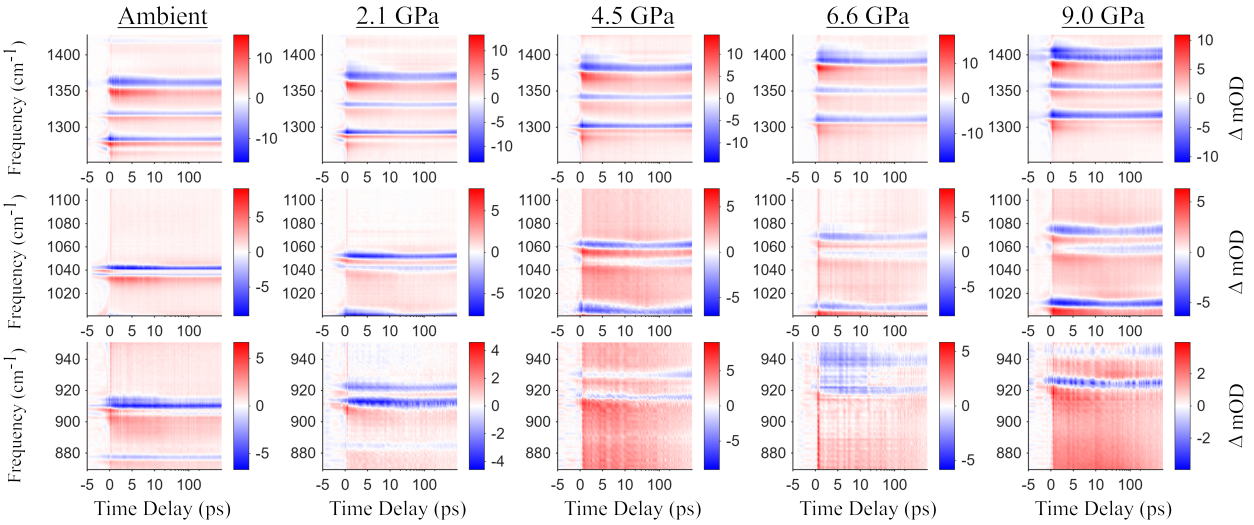

Figure 2: Transient absorption spectra of BNFF from ambient pressure to 9.0 GPa, with 1675 cm^{-1} vibrational excitation occurring at time t=0. Time delays are linear from -5 ps to 10 ps, and then logarithmic from 10 ps to 300 ps. See SI section S1.2 for experimental details.

changes on the $\mathcal{O}$(100 ps) timescale suggest evolution of the phonon bath, and appears more prominently at higher pressures due to stronger intermolecular interactions imposed by the static compression. Further inspection of Figure 2 shows that some bleach features become enveloped by the pressure-induced broadening of neighboring induced absorption features, such as the 1038 cm^{-1} mode at ambient pressure.

Overall, the dynamics accelerate with increasing hydrostatic pressure, although the trend is linearly related to applied pressure for only τ_2, which represents the $\mathcal{O}$(1 ps) global vibrational relaxation, where there is a ∼-0.9 ps/GPa acceleration of VET vs increasing pressure with an $R^2 = 0.87$. The τ_3 lifetime, which is the $\mathcal{O}$(100 ps) evolution of the phonon bath, displays a clear acceleration at elevated pressures compared to ambient condition, but does not exhibit a trend at higher pressures. The τ_1 lifetime corresponds to the $\mathcal{O}$(sub-ps) dynamics and shows no correlation even between ambient vs pressurized datasets, likely because τ_1 is too close to the experimental IRF to be reliably measured.

The acceleration of the $\mathcal{O}$(1 ps) vibrational relaxation at elevated pressures is visually depicted in Figure 3. We can rationalize this behavior using two potential, non-mutually

Table 1: Time Constants (ps) from the Global Lifetime Analysis of the Transient Data.

Pressure	τ_1	τ_2	τ_3	τ_4
Ambient	0.054	9.07	754	10^6 (fixed)
2.1 GPa	0.331	7.86	711	10^6 (fixed)
4.5 GPa	0.576	8.33	198	10^6 (fixed)
6.6 GPa	0.248	6.51	649	10^6 (fixed)
9.0 GPa	0.057	5.35	573	10^6 (fixed)

exclusive frameworks. First, in the multi-phonon up-pumping model, the density of doorway modes may increase with pressure, resulting in more available pathways for scattering. Indeed, from the DFT results shown in Figs. S5 and S6, it is seen that nearly all probed vibrations show consistent increases in the number of scattering events through modes in the *Doorway* ($\omega_{max} < w < 2\omega_{max}$) range with increasing pressure. These values are the product between the count of available scattering events and the strength of coupling among the modes involved. By integrating this quantity in selected windows of the total vibrational spectrum and normalizing by the count of normal modes (Figs. S7 and S8 and Supplemental Table S3), we find that *Doorway* modes are most sensitive to pressure changes. Because these states facilitate coupling between the phonon bath and the high frequency intramolecular vibrations, a higher density of active doorway states may explain the faster VET. Labels on other windows reflect common nomenclature, and are not rigorously defined. Alternatively, the observed pressure-induced acceleration of vibrational relaxation could result from an increase in delocalization of the high-frequency vibrational modes as a result of increased intermolecular interaction strength. This could lead to an enhanced direct coupling between high-frequency modes and low-frequency modes.[22,23,28,29] Presently, we are not able to predict changes in delocalization with pressure, as this necessitates computationally prohibitive larger simulation cells.

Both the $\mathcal{O}$(sub-ps) and $\mathcal{O}$(100 ps) time constants do not display a linear trend with pressure, with R^2 values of 0.003 and 0.09 respectively from a linear regression. While the change in the integrated joint density of states (ΔJDoS) is best used to explain the $\mathcal{O}$(1

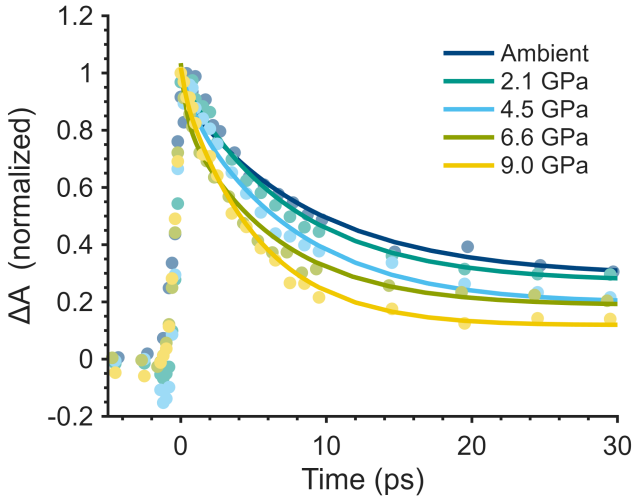

Figure 3: Transient behavior from -2 to 30 ps for the symmetric N-O-N ring deformation vibration (1347 cm^{-1} at ambient pressure) as the DAC pressure is increased to 9.0 GPa. Experimentally measured changes in absorption as a function of pump-probe delay (markers) and the global analysis sequential kinetic model fits (solid lines) are both normalized to the maximum of the experimental data. Fits are shifted by (in ascending order of pressure) -0.3, -0.5, -0.5, -0.7, and -0.5 ps to account for subtle offsets in the location of time-zero. There is a steady increase in vibrational relaxation rate as pressure is increased.

ps) relaxation, it is inconclusive for explaining the mode-specific dynamics on the $\mathcal{O}$(100 ps) timescale. Pressure-driven changes in scattering with any of the integrated spectral ranges shown in Figs. S7 and S8 and Supplemental Table S3 do not trend with the observed mode-specific $\mathcal{O}$(100 ps) pressure sensitivity. However, this analysis does illustrate that modes closer in frequency to the phonon bath generally appear to undergo more scattering events than higher frequency modes, and higher frequency modes have flatter scattering curves vs frequency. There are a few high-frequency vibrations (e.g. ModeID = 225, 239) that show that the *Fingerprint* window is just as pressure sensitive as the doorway modes. ModeID = 225 is noted as one of the modes with the most pressure sensitive dynamics on $\mathcal{O}$(100 ps), assigned as a CC + CN stretch in the less sterically hindered furazan ring.

Figure 4 illustrates the symmetric N-O-N furazan ring deformation (1347 cm^{-1} at ambient pressure) vibrational mode's transient behavior which, at ambient pressure, shows minimal participation in the $\mathcal{O}$(100 ps) evolution. However, under increased pressure, this mode acquires an active long-time component. This trend is not uniform across modes un-

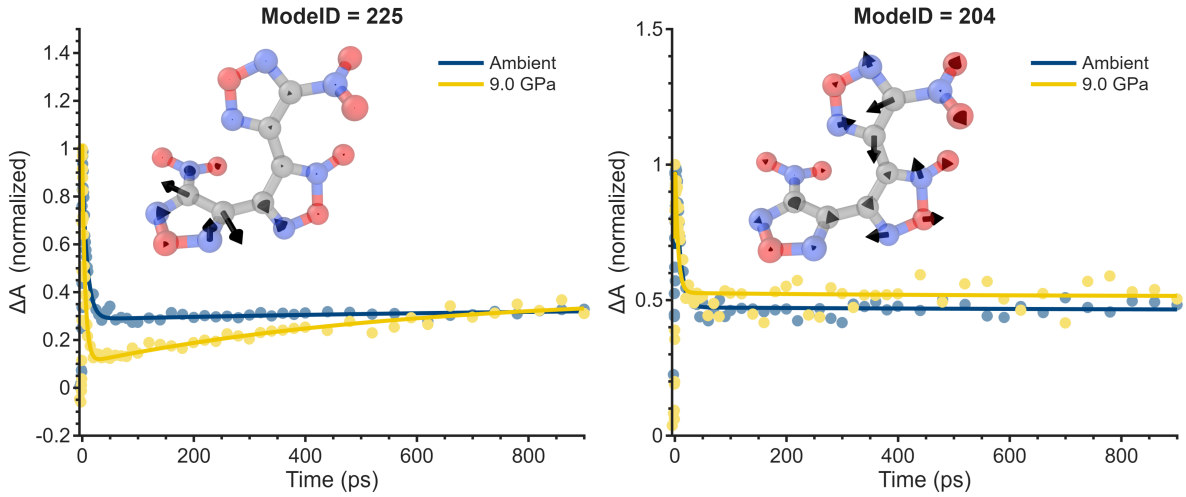

Figure 4: Transient behavior from -5 to 900 ps for both the symmetric N-O-N ring deformation vibration (**Left** - 1347 cm^{-1} at ambient pressure) and the C-C-N Angle + N-O-N Angle vibration (**Right** - 1126 cm^{-1} at ambient pressure) as the DAC pressure is increased to 9.0 GPa. The left mode was non-participatory in the $\mathcal{O}$(100 ps) dynamics at ambient pressure, yet becomes "activated" under high static pressure conditions, while the right mode remains non-participatory.

der visual inspection, with some exhibiting little to no change in long-time dynamics with pressure, such as the time evolution of the 1126 cm^{-1} mode shown in the right panel of Figure 4. Quantifying these observations while accounting for scaling differences across modes with different oscillator strengths is challenging, and alternative approaches may achieve better insights (see S5.2). Our analysis finds that the modes at 1126 cm^{-1}, 1318 cm^{-1}, and 1176 cm^{-1} show minimal changes in their long time evolution with pressure. However, most modes indeed acquire $\mathcal{O}$(100 ps) character under pressure, or "activate". The modes at 1042 cm^{-1}, 906 cm^{-1}, and 1356 cm^{-1} exhibit the most pronounced activation under pressure. By using optimized molecular structures and normal mode displacements calculated by DFT, metrics of mode character were evaluated as described in the SI (section S5.3), such as mode localization, total mode displacement, nitro/furazan character, and mode weighted nearest neighbor distances. These analyses reveal that pressure-sensitive modes are generally more localized and exhibit smaller total atomic displacements compared to pressure-insensitive modes. Pressure-insensitive modes are found to have strong carbon backbone or nitro-group character, while pressure-sensitive modes are significantly localized to the furazan ring away

from the protruding furoxan N-O group as illustrated in Figure S19. The heightened sensitivity of the $\mathcal{O}$(100 ps) lifetime in the less-sterically crowded furazan O-N-O ring vibrations is particularly interesting, as cleavage of furazan O-N-O rings is suspected to initiate BNFF decomposition.[30,31] If the furazan O-N-O ring cleavage is indeed the first step in detonation, its particular sensitivity to shockwave-relevant pressures as an exacerbating molecular property could inform future energetic material design. However, this pressure-dependent activation represents an experimentally observed signature of long-time vibrational energy redistribution that is not captured by existing theoretical frameworks such as the multi-phonon up-pumping model or recent nonequilibrium kinetic models[24] alone.

In summary, our joint experiment-theory work explores the effects of high static pressure, and therefore intermolecular interaction strength, on the vibrational energy transfer dynamics of a hydrogen-free energetic material for the first time. We find that VET accelerates under pressure, with vibrational relaxation in particular displaying a near-linear pressure dependence, indicating intermolecular interaction strength plays a prominent role in VET dynamics. Additionally, select vibrational modes continue to evolve over timescales extending to 900 ps, suggesting incomplete VET well beyond the timescales predicted by the multi-phonon up-pumping model. The $\mathcal{O}$(100 ps) evolution of the furazan O-N-O ring vibrational modes is particularly influenced by pressure, indicating a higher sensitivity to lattice compression. This enhanced coupling of detonation-relevant moieties to lattice modes under shockwave-like conditions provides new insights into the interplay between molecular design and inter-/intramolecular couplings, paving the way for a mechanistic understanding of impact sensitivity in energetic material design.

Methods

BNFF thin film samples were produced by physical vapor deposition onto CaF_2 and diamond anvil substrates. The thickness was controlled by the amount of starting material loaded

into the high-vacuum system, and the morphology of the resulting films was characterized via scanning electron microscopy and X-ray diffraction. Static FTIR measurements were performed on ∼2-3 μm thin films using a commercial FTIR system. Ultrafast broadband IR measurements were performed on ∼ 2-3 μm thick BNFF thin films using our apparatus (SI). Briefly, a commercial Ti:Sapphire laser system pumps an optical parametric amplifier, whose signal and idler outputs are difference frequency mixed in a 0.5 mm thick $AgGaS_2$ crystal. This produces a tunable, narrowband IR pulse (∼ 2-4 μJ, ∼40 fs) optimized to excite the 1640 cm^{-1} furoxan N-O asymmetric stretch vibrational mode of BNFF. Additionally, the Ti:Sapphire system drives a plasma-based source of broadband infrared pulses, which covers all IR-active vibrational modes of BNFF. The DAC is a symmDAC from Almax easyLab, with an 800 μm diameter culet size, allowing for pressures of up to 12 GPa. Pre-indented stainless steel gaskets were used with a drilled hole of 310 μm diameter. Argon is loaded into the DAC in liquid form under cryogenic conditions and acts as the pressure transmitting medium.

DFT was applied to BNFF to enable vibrational mode assignments and calculate the two-phonon density of states. Computational assignments of mode character and scattering pathways are made using the Finite Displacement Supercell (FDS) method up to the first anharmonic moment of the potential energy. This involves symmetry reduced displacements of atom pairs in cartesian directions where forces are collected into the dynamical matrix where a diagonalization yields normal modes, and force constants up to second order. We utilize Phono3py to streamline the process of generating displacements and analysis of joint density of states, and CP2K for first principles predictions of forces due to the availability of hybrid atomic and plane wave basis sets. All individual FDS calculations were performed on the geometry (cell and atom positions) optimized BNFF unit cell (88 atom) structures at the desired pressures (1 atm, 4GPa, 10GPa). Unit cell volume and position of asymmetric N-O stretch mode at 1 atm of pressure were used as validation points with respect to experiments for our choice of basis and pseudo-potential choices. For reproducibility, our exact inputs can

be found at https://cp2k-basis.pierrebeaujean.net/ using 'TZVP-MOLOPT-PBE-GTH' for Basis Set, and 'GTH-PBE' for pseudo-potential definition. A 2x2x2 Monkhorst-Pack k-point mesh was used with a 1200Ry kinetic energy cutoff on the plane-wave basis set. Additionally, a D3(BJ) van der Waals corrected PBE functional was used with Broyden Mixing of $\alpha = 0.4$ to achieve convergence to 10^{-6} within 50 SCF steps for all calculations. Optimized structures are available in the SI as inputs to CP2K containing all of these parameter choices.

Obtaining the harmonic and anharmonic force constants gives us the ability to predict VET by simply applying Fermi's Golden Rule to pumped modes. We consider VET up to the interaction of three phonons, for example the collision of two vibrations resulting in the elevation of the population of a third. Constraints on the predicted JDOS are applied via the conservation of crystal momentum and total energy. Due to the dense vibrational spectrum characteristic of molecular crystals, the JDOS will predict scattering events for nearly all frequencies between zero-frequency translation/rotation and twice the highest frequency modes (asymmetric NO stretch). Data shown in Fig. S5 and Fig. S6 is collected by first applying a gaussian perturbation to the Bose-Einstein distribution centered on the vibration of interest. Subtracting the JDOS predicted from thermal occupation of all modes gives the set of scattering events coupled to the pumped mode. Finally, this JDOS difference is multiplied by a binary filter representing the presence of available native vibrations in BNFF to accept the scattering event, integrating through frequency gives the final data.

Further details on the theoretical methods, experimental apparatus, and sample preparation/characterization can be found in the SI.

Acknowledgement

The authors would like to thank Dave Boruta, Paul Gianuzzi, and Brad Sleadd, ret. (Naval Surface Warfare Center, Indian Head, MD), and Phil Samuels (DEVCOM Armaments Cen-

ter, Picatinny Arsenal, NJ) for providing the BNFF, Michael Marquez (Sandia National Laboratories, Albuquerque, NM) for performing the BNFF thin-film depositions, and Will Bassett (Sandia National Laboratories, Albuquerque, NM) and Alex Tappan (Sandia National Laboratories, Albuquerque, NM) for helpful discussions. This work was supported by the Laboratory-Directed Research and Development Program at Sandia National Laboratories. Sandia National Laboratories is a multi-mission laboratory managed and operated by National Technology Engineering Solutions of Sandia, LLC (NTESS), a wholly owned subsidiary of Honeywell International Inc., for the U.S. Department of Energy's National Nuclear Security Administration (DOE/NNSA) under contract DE-NA0003525. This written work is authored by employees of NTESS. The employees, not NTESS, owns the right, title and interest in and to the written work and is responsible for its contents. Any subjective views or opinions that might be expressed in the written work do not necessarily represent the views of the U.S. Government. The publisher acknowledges that the U.S. Government retains a non-exclusive, paid-up, irrevocable, world-wide license to publish or reproduce the published form of this written work or allow others to do so, for U.S. Government purposes. The DOE will provide public access to results of federally sponsored research in accordance with the DOE Public Access Plan.

Supporting Information Available

Details of the sample preparation; experimental and theoretical methods; theoretical results; additional experimental results; discussion of kinetic modeling and fitting; and details and discussion of analysis of the long-time dynamic

References

(1) Tsyshevsky, R. V.; Sharia, O.; Kuklja, M. M. Molecular Theory of Detonation Initiation: Insight from First Principles Modeling of the Decomposition Mechanisms of

Organic Nitro Energetic Materials. *Molecules* **2016**, *21*, 236, Number: 2 Publisher: Multidisciplinary Digital Publishing Institute.

(2) Yan, Q.-L.; Zeman, S. Theoretical evaluation of sensitivity and thermal stability for high explosives based on quantum chemistry methods: A brief review. *International Journal of Quantum Chemistry* **2013**, *113*, 1049–1061, _eprint: https://onlinelibrary.wiley.com/doi/pdf/10.1002/qua.24209.

(3) Dlott, D. D.; Fayer, M. D. Shocked molecular solids: Vibrational up pumping, defect hot spot formation, and the onset of chemistry. *The Journal of Chemical Physics* **1990**, *92*, 3798–3812.

(4) Tokmakoff, A.; Fayer, M. D.; Dlott, D. D. Chemical reaction initiation and hot-spot formation in shocked energetic molecular materials. *The Journal of Physical Chemistry* **1993**, *97*, 1901–1913, Publisher: American Chemical Society.

(5) Michalchuk, A. A. L.; Trestman, M.; Rudić, S.; Portius, P.; Fincham, P. T.; Pulham, C. R.; Morrison, C. A. Predicting the reactivity of energetic materials: an ab initio multi-phonon approach. *Journal of Materials Chemistry A* **2019**, *7*, 19539–19553, Publisher: The Royal Society of Chemistry.

(6) Michalchuk, A. A. L.; Hemingway, J.; Morrison, C. A. Predicting the impact sensitivities of energetic materials through zone-center phonon up-pumping. *The Journal of Chemical Physics* **2021**, *154*, 064105.

(7) Bernstein, J. *Ab initio* study of energy transfer rates and impact sensitivities of crystalline explosives. *The Journal of Chemical Physics* **2018**, *148*, 084502.

(8) Bondarchuk, S. V. Theory of impact sensitivity revisited: mechanical-to-vibrational energy transfer phenomenon. *FirePhysChem* **2022**, *2*, 334–339.

(9) Bao, S.-Y.; Liu, Q.-J.; Hong, D.; Liu, W.-H.; Ma, X.-J.; Liu, F.-S.; Xing, W.; Liu, Z.-T. To explore the relationship between energy transfer rate and impact sensitivity by the first-principle calculation method. *Journal of Physics and Chemistry of Solids* **2023**, *177*, 111298.

(10) Liu, W.-H.; Zeng, W.; Liu, F.-S.; Liu, Z.-T.; Liu, Q.-J. Probing into the theory of impact sensitivity: propelling the understanding of phonon–vibron coupling coefficients. *Physical Chemistry Chemical Physics* **2024**, *26*, 7695–7705, Publisher: Royal Society of Chemistry.

(11) Chen, S.; Tolbert, W. A.; Dlott, D. D. Direct Measurement of Ultrafast Multiphonon Up-Pumping in High Explosives. *The Journal of Physical Chemistry* **1994**, *98*, 7759–7766, Publisher: American Chemical Society.

(12) Dlott, D. D. ULTRAFAST SPECTROSCOPY OF SHOCK WAVES IN MOLECULAR MATERIALS. *Annual Review of Physical Chemistry* **1999**, *50*, 251–278, Publisher: Annual Reviews.

(13) Ostrander, J. S.; Knepper, R.; Tappan, A. S.; Kay, J. J.; Zanni, M. T.; Farrow, D. A. Energy Transfer Between Coherently Delocalized States in Thin Films of the Explosive Pentaerythritol Tetranitrate (PETN) Revealed by Two-Dimensional Infrared Spectroscopy. *The Journal of Physical Chemistry B* **2017**, *121*, 1352–1361, Publisher: American Chemical Society.

(14) Ren, H.; Ji, L.; Jia, X.; Tao, J.; Liu, R.; Wei, D.; Wang, X.; Ji, G. Theoretically Revealing the Response of Intermolecular Vibration Energy Transfer and Decomposition Process of the DNTF System to Electric Fields Using Two-Dimensional Infrared Spectra. *International Journal of Molecular Sciences* **2023**, *24*, 4352, Number: 5 Publisher: Multidisciplinary Digital Publishing Institute.

(15) Shi, L.; Yu, P.; Zhao, J.; Wang, J. Ultrafast Intermolecular Vibrational Energy Transfer

in Hexahydro-1,3,5-trinitro-1,3,5-triazine in Molecular Crystal by 2D IR Spectroscopy. *The Journal of Physical Chemistry C* **2020**, *124*, 2388–2398, Publisher: American Chemical Society.

(16) Franken, J.; Hambir, S.; Hare, D.; Dlott, D. Shock waves in molecular solids: ultrafast vibrational spectroscopy of the first nanosecond. *Shock Waves* **1997**, *7*, 135–145.

(17) McGrane, S. D.; Moore, D. S.; Funk, D. J. Shock Induced Reaction Observed via Ultrafast Infrared Absorption in Poly(vinyl nitrate) Films. *The Journal of Physical Chemistry A* **2004**, *108*, 9342–9347, Publisher: American Chemical Society.

(18) Powell, M. S.; Sakano, M. N.; Cawkwell, M. J.; Bowlan, P. R.; Brown, K. E.; Bolme, C. A.; Moore, D. S.; Son, S. F.; Strachan, A.; McGrane, S. D. Insight into the Chemistry of PETN Under Shock Compression Through Ultrafast Broadband Mid-Infrared Absorption Spectroscopy. *The Journal of Physical Chemistry A* **2020**, *124*, 7031–7046, Publisher: American Chemical Society.

(19) Powell, M. S.; Moore, D. S.; McGrane, S. D. Insight into the chemistry of TNT during shock compression through ultrafast absorption spectroscopies. *The Journal of Chemical Physics* **2021**, *154*, 054201.

(20) Ramasesha, K.; Wood, M.; Cole-Filipiak, N. C.; Knepper, R. *Experimental and Theoretical Studies of Ultrafast Vibrational Energy Transfer Dynamics in Energetic Materials*; 2020.

(21) Cole-Filipiak, N. C.; Knepper, R.; Wood, M.; Ramasesha, K. Sub-picosecond to Sub-nanosecond Vibrational Energy Transfer Dynamics in Pentaerythritol Tetranitrate. *The Journal of Physical Chemistry Letters* **2020**, *11*, 6664–6669, Publisher: American Chemical Society.

(22) Cole-Filipiak, N. C.; Knepper, R.; Wood, M.; Ramasesha, K. Mode-Selective Vibrational Energy Transfer Dynamics in 1,3,5-Trinitroperhydro-1,3,5-triazine (RDX) Thin

Films. *The Journal of Physical Chemistry A* **2021**, *125*, 7788–7802, Publisher: American Chemical Society.

(23) Kraczek, B.; Chung, P. W. Investigation of direct and indirect phonon-mediated bond excitation in alpha-RDX. *The Journal of Chemical Physics* **2013**, *138*, 074505.

(24) Liu, Z.; Batyrev, I. G.; Byrd, E. F. C.; Chung, P. W. A nonequilibrium kinetic model of high-resolution vibrational energy transfer in RDX from selective IR excitation. *The Journal of Chemical Physics* **2024**, *161*, 224703.

(25) Strachan, A.; van Duin, A. C.; Chakraborty, D.; Dasgupta, S.; Goddard III, W. A. Shock waves in high-energy materials: The initial chemical events in nitramine RDX. *Physical Review Letters* **2003**, *91*, 098301.

(26) Zhang, B.; Yang, K.; Liu, D.; Xiao, Y.; Zhang, K.; Yang, T.; Lu, J.; Wu, J.; Chen, L. Development of Reactive Force Field for DNTF and Molecular Dynamics Simulation of Reaction Mechanism under Shock Loading. *The Journal of Physical Chemistry C* **2024**, *128*, 4958–4968, Publisher: American Chemical Society.

(27) Nan, H.; Su, H.; Chen, C.; Bu, Y.; Niu, G.; Sun, P.; Shen, F.; Wang, X. Infrared spectra and electronic structural changes of DNTF under high pressure: experimental and theoretical studies. *Physical Chemistry Chemical Physics* **2024**, *26*, 9517–9523, Publisher: Royal Society of Chemistry.

(28) Coffey, C. S.; Toton, E. T. A microscopic theory of compressive wave-induced reactions in solid explosives. *The Journal of Chemical Physics* **1982**, *76*, 949–954.

(29) Zerilli, F. J.; Toton, E. T. Shock-induced molecular excitation in solids. *Physical Review B* **1984**, *29*, 5891–5902, Publisher: American Physical Society.

(30) Tsyshevsky, R. V.; Kuklja, M. M. Decomposition Mechanisms and Kinetics of Novel Energetic Molecules BNFF-1 and ANFF-1: Quantum-Chemical Modeling. *Molecules*

2013, *18*, 8500–8517, Number: 7 Publisher: Multidisciplinary Digital Publishing Institute.

(31) Tsyshevsky, R.; Pagoria, P.; Zhang, M.; Racoveanu, A.; DeHope, A.; Parrish, D.; Kuklja, M. M. Searching for Low-Sensitivity Cast-Melt High-Energy-Density Materials: Synthesis, Characterization, and Decomposition Kinetics of 3,4-Bis(4-nitro-1,2,5-oxadiazol-3-yl)-1,2,5-oxadiazole-2-oxide. *The Journal of Physical Chemistry C* **2015**, *119*, 3509–3521, Publisher: American Chemical Society.

Supporting Information

The Effects of Shockwave Pressures on Ultrafast Vibrational Energy Transfer in BNFF, a Hydrogen-Free Energetic Material

Daniel Carlson,[†] River Leversee,[‡] Paul Schrader,[†] Kendrew Au,[†] Robert Knepper,[¶] Mitchell Wood,[*,§] and Krupa Ramasesha[*,†]

[†]*Combustion Research Facility, Sandia National Laboratories, Livermore, California 94550, United States*

[‡]*University of Colorado, Boulder, Colorado 80309, United States*

[¶]*Explosive Technologies Group, Sandia National Laboratories, Albuquerque, New Mexico 87185, United States*

[§]*Center for Computing Research, Sandia National Laboratories, Albuquerque, New Mexico 87185, United States*

E-mail: mitwood@sandia.gov; kramase@sandia.gov

S1 Methods

S1.1 Sample Preparation

BNFF films were deposited in a custom high vacuum chamber onto CaF_2 and diamond anvil substrates using vacuum thermal evaporation from an effusion cell deposition source. Deposition was performed at a base pressure of approximately 10^{-6} Torr, and a shadow mask was used to define the deposition area. Film thickness was controlled by the amount of material loaded into the source, generally ranging from 2 - 5 μm. Morphology of the resulting films was characterized via scanning electron microscopy (Zeiss GeminiSEM 300) and X-ray diffraction (Rigaku MiniFlex). SEM samples were coated with a thin ($\sim$5 nm) layer of iridium prior to imaging to mitigate charging effects, and imaging was performed using a 1.1 kV accelerating voltage. Images of both the top surface and fracture cross-section are shown below. Results show very low surface roughness and a sub-micron typical grain size. θ-2θ x-ray diffraction scans were performed at a rate of 10 degrees/minute and a step size of 0.01 degrees to interrogate sample crystal structure and any preferred orientation. The diffraction pattern matches well with the reported orthorhombic crystal structure, and the relative peak intensities suggest that the grain structure is largely randomly oriented.

S1.2 Experimental Methods

A commercial Ti:Sapphire amplified laser system (Legend Elite Duo HE, Coherent) operating at 1 kHz, 800 nm center wavelength, and 40 fs pulse duration has a 10 mJ output and a 3 mJ output arm, which are used to generate the narrowband IR pump and broadband IR probe pulses, respectively. The 10 mJ output pumps a commercial optical parametric amplifier (HE-TOPAS Prime Plus, Light Conversion), which generates spatially and temporally overlapped signal and idler with 4 mJ of combined pulse energy and center wavelengths of $\sim$1425 nm and $\sim$1818 nm, respectively. This beam is then sent unfocused through an $AgGaS_2$ crystal for difference frequency generation of the mid-IR pump pulse centered at

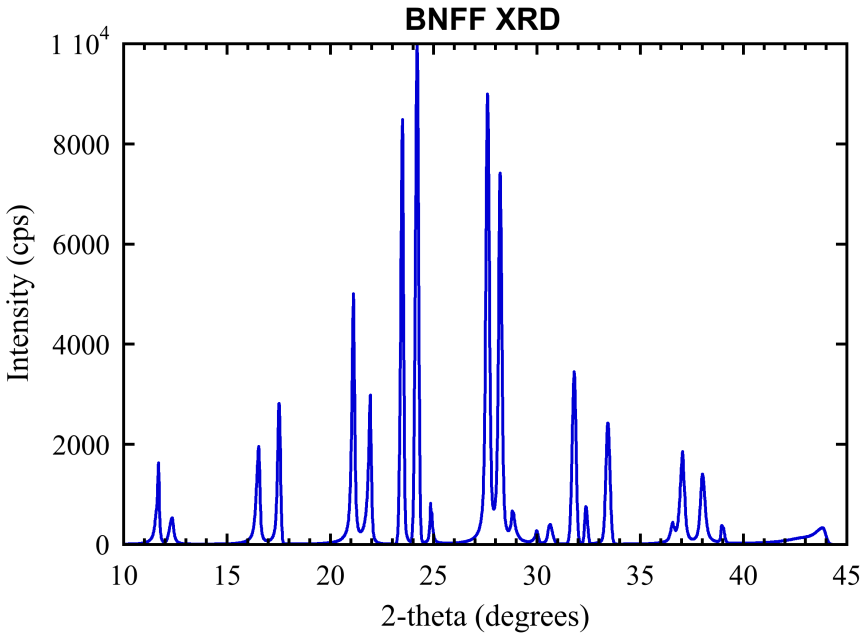

Figure S1: θ-2θ x-ray diffraction with relative peak intensities suggesting a random orientation for the underlying grain structure.

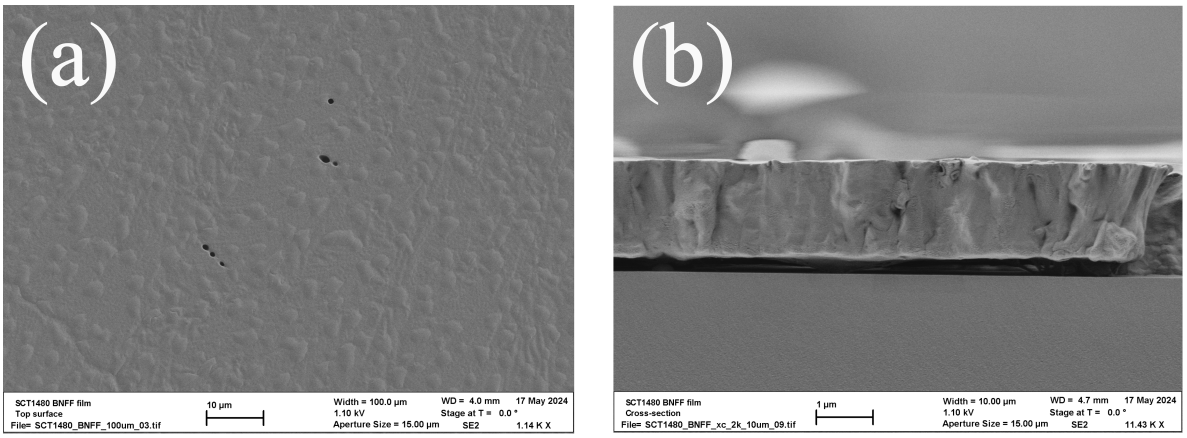

Figure S2: Scanning electron microscopy of BNFF samples showing low surface roughness and a sub-micron typical grain size. (a) Top-down view and (b) fracture cross section of a thin film.

1640 cm^{-1}, and its bandwidth is further narrowed by a band pass filter centered at 1667 cm^{-1} with a full-width-at-half-maximum bandwidth of ∼150 cm^{-1}.

The 3 mJ output is attenuated to 1.5 mJ and temporally delayed with respect to the narrowband IR pump arm using a combination of two different motorized delay stages. One stage (Aerotech ANT95L-050-MP-PL2-TAS, 50 mm travel length) scans the delay with fine time steps in 320 ps temporal windows, while another stage (Newport ILS200HA, 200mm travel length) applies either a 0 ps, 300 ps, or 600 ps temporal offset to achieve the large temporal sampling range of -15 to 900 ps for the experiment. This beam is then frequency doubled with a Type 1 β-barium borate crystal and sent through a dual waveplate and delay compensation plate. The dual waveplate rotates the 800 nm polarization to match the 400 nm, and the compensator plate corrects for temporal drift from the waveplate. The two colors are then sent through a final BBO crystal to generate co-propagating 266 nm, and all three colors are then tightly focused with a 0° dielectric coated concave mirror with a focal length of 5 cm. A gentle laminar flow of nitrogen gas is centered on the focal spot and a plasma is formed. From this plasma, supercontinuum IR is generated[1–3] and collimated, and then sent through a 0.5 mm thick, undoped Si(100) wafer to selectively pass only the mid-IR wavelengths. This broadband IR probe spans 800-4000 cm^{-1} with ∼15 nJ per pulse, measured with a Newport 919P-003-10 thermopile power sensor and 843-R laser power meter.

The pump and probe pulses are separated vertically and sent onto a 3-inch, gold-coated, 90° off-axis parabola (OAP) with an effective focal length of 101.6 mm. At the focal plane, the pump beam has a ∼320 μm $1/e^2$ beam diameter and the probe beam has a ∼220 μm $1/e^2$ beam diameter as measured via power transmission through a 100 μm diameter pinhole, and they cross at a ∼53° angle. The transmitted probe beam is then collimated by a matching 1-inch diameter OAP and focused into a liquid nitrogen-cooled, 64-element, HgCdTe array detector (Infrared Systems Development Corporation). A 50 lines/mm grating is used for this experiment which provides a 15.2573 nm/pixel spectral resolution and collects data in 1000 nm windows. For the 6, 6.5, and 7 μm spectral windows, pump scatter was minimized by

using a smaller collimating OAP that selectively catches the probe beam after the sample, the pump and probe beams were cross-polarized, and a ZnSe wire-grid polarizer was installed in front of the spectrometer to pass the probe beam polarization. Furthermore, an iris centered on the probe beam further mitigated pump scatter. A long-pass filter is used to eliminate higher-order diffraction in the long probe wavelength acquisition windows; a 4.5 μm long-pass filter is used for the 6-8 μm windows, and a 7.3 μm long-pass filter is used for the 8.5+ μm windows.

A 3D translation stage is installed to manipulate samples at the focal plane of the OAP. Initially, a 100 μm diameter pinhole is placed at the focus by moving the pinhole until maximizing probe transmission is achieved. Then, the pump beam transmission is maximized by adjusting the beam pointing. Thus, the pump and probe are spatially overlapped before the DAC is inserted, with final minor tweaks of the pump position done to maximize signal after DAC insertion. The instrument response function (IRF) is measured in a 0.5 mm thick undoped InSb(100) wafer; the FWHM IRF was found to be $\sim$400 fs.

The entire apparatus is enclosed in an optical box and purged with dry N_2 to minimize IR-absorption from propagation through air. Time delays are randomly sampled within each 300 ps temporal sub-window to avoid systematic errors from pulse energy drifts during the experiment. Each temporal data point is an average of 5000 laser shots. The 300 ps temporal sub-windows are stitched together in post-processing. A data set at each pressure requires about 6 hours to acquire.

S1.3 Theoretical Methods

High pressure structure optimization was performed using the CP2K Cell Opt calculation type. The starting structure for all high pressure optimizations was the optimized structure at ambient conditions. The structure was optimized for target pressures of 4 GPa and 10 GPa while constraining the structure to an orthorhombic unit cell. Initial poor convergence was observed for pressures greater than 4 GPa, which was remedied by setting a

higher Broyden mixing term to 0.4 and utilizing molecularly optimised (MOLOPT) basis sets. These minimum energy structures are the starting point for the finite-displacement supercell (FDS) calculations that expand the potential energy surface to harmonic and first anharmonic moment. A set of calculations is performed where forces on all atoms are collected after a single (harmonic) or pair (anharmonic) of displacements are made. Ideally, PhonoPy can identify symmetry reductions where some displacements are degenerate, reducing the number of individual calculations needed. However, even the energy-minimized structures of these molecular crystals necessitated a full detail of displacements, which is a total of 528 calculations for harmonic and 279,312 calculations per pressure for anharmonic force constant construction. Given the large computational expense in gathering these force constants, they are available upon request.

Given the force constants collected from FDS calculations that define the interacting vibrations of the material, we now turn to sampling of the density of states. Here a Fourier transform of the real-space force constants is done to in-turn sample from a regular k-space grid of the Brillion Zone. A 4x4x4 grid is used to sample the one-phonon density of states, no changes were seen for denser grids.It is important to note that the predicted DoS includes both Raman and IR active modes in the material.Born effective per-atom charges are taken from the ground-state structures at each pressure which are projected onto normal modes of the system to determine dipole intensities for each mode. A denser 10x10x10 grid was used for calculating the two-phonon DoS, which we refer to as the joint density of states (JDOS). The JDOS predicts the spectrum of two-phonon collisions and represents all possible pathways for vibrational energy transfer (VET) to occur in the system. Equation S1 defines the JDOS as the set of two-phonon collisions that satisfy Fermi's Golden Rule, ie. those that preserve energy, momentum in the crystal, and are scaled by the interaction strength (anharmonic

coupling).

$$\Gamma(\omega) = \sum_{\omega'\omega''} |\Phi_{\omega\omega'\omega''}|\delta(q - q^{'} - q^{''})[(n_{\omega'} + n_{\omega''} + 1)\delta(\omega - \omega^{'} - \omega^{''}) + (n_{\omega'} - n_{\omega''})(\delta(\omega + \omega^{'} - \omega^{''}) - \delta(\omega - \omega^{'} + \omega^{''}))] \tag{S1}$$

In Eq. S1, n_ω is the Bose-Einstein occupation of mode ω, q the wave vector, and $\Phi_{\omega\omega'\omega''}$ the coupling strength between $\omega^{'}$ and $\omega^{''}$ scattering into ω. The inverse of $\Gamma(\omega)$ is the phonon lifetime. While the Kroneker deltas, δ, will suppress many possible combination of modes, there are still 264 normal modes and 10,000 k-points where phonon collisions are possible, yielding a dense JDOS. To emulate the experimental pump-probe setup, we calculate differences in JDOS (ΔJDOS) with respect to thermal occupation where changes to the mode occupation, n, are targeted to modes of interest. As one last step in analyzing the VET from the ΔJDOS, we multiply the ΔJDOS by a binarized (one or zero) version of the one-phonon DoS in order to screen for scattering events that result in a change in occupation of a native vibration in BNFF.

S2 Theoretical Results

Table S1: Optimized BNFF cell lengths at each of the tested pressures using CP2K Cell Opt function.

Pressure	a(Å)	b(Å)	c(Å)	Volume(Å^3)
Ambient	6.738	10.971	15.262	1128.21
4GPa	6.115	10.569	14.505	937.45
10GPa	5.771	10.343	14.012	836.37
Ambient Ref[4]	7.147	9.790	15.277	1068.90

Beginning with the predicted static properties of BNFF, Table S1 gathers the cell dimensions at each of the pressures tested. Our data is in good agreement with available literature, with error in the density at ambient conditions equal to 5.5%.

S2.1 Vibrational Modes of Crystalline BNFF

Predicted IR spectra at each pressure are displayed in Figure S3, where modes of predominately N-O character are seen to have the strongest signal. Lorentzian linewidths are analytically added to the computed IR spectra corresponding to T=300K. The spectra between experiment and theory are in good agreement, and a specific subset of modes have been highlighted in Table S2 for a detailed comparison. Calculated frequencies are given for ambient (top), 4 GPa (middle), and 10 GPa (bottom), and experimental frequencies are given for ambient (top), 4.5 GPa (middle), and 9 GPa (bottom). Additional information displayed in this table are the mass-weighted displacement vectors of the normal mode with descriptions of the mode given in the Assignment column. These normal modes are calculated from the unit cell (four molecules) but for clarity vector projections are shown for a representative single molecule. As discussed in the Results & Discussion section, we identified key characteristics of modes based on their $\mathcal{O}$(100ps) relaxations, these are also included in the assignments. Lastly, the total displacement of the normal mode (indexed as ModeID) projection is broken down by element type. We did not observe dramatic shifting of normal mode frequencies relative to one another, allowing us to preserve the normal mode indexes thru pressure. As one might expect, we observed with increasing frequency that normal mode displacements become more intra-molecular and include fewer atoms in their motion. This is observed clearly for ModeID$\geq$225 in Table S2. While not discernible from the displacement vectors in Table S2, the four molecule unit cell only permits short wavelength delocalization. Often we observed that two molecules displayed displacements in phase while the other pair where out of phase by $\pi/2$. The computational expense of constructing anharmonic force constants ($\simeq 3 \cdot 10^5$ converged DFT calculations) means it would have been prohibitively expensive to extend this analysis to a supercell of the molecular crystal. However, the same analysis can be replicated where atomic forces are produced by cheaper alternative like a classical interatomic potential. This is beyond the scope of the present work, but should be undertaken by the entrepreneurial reader.

Table S2: Mode assignments from DFT with corresponding experimental data and labels

Displacements	**Calc. Freq.** (cm^{-1})	**Expt. Freq.** (cm^{-1})	**Assignment**	**Character**
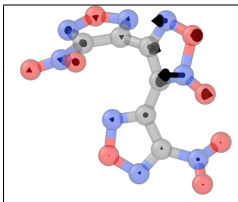 ModeID=120	557.1 562.4 566.0	N/A	Ring Twist	C: 0.2434 N: 0.4285 O: 0.3281 IR: 0.3736
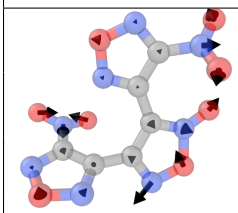 ModeID=166	808.1 817.3 827.6	806.212 816.82 820.677	NO_2 Sym. Stretch + NONO dihedral, (Low.Press.Sens. of $\mathcal{O}$(100ps))	C: 0.1188 N: 0.3522 O: 0.5291 IR: 0.2971
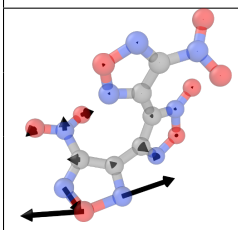 ModeID=172	819.5 830.2 843.7	825.499 830.803 834.179	Ring NO asym. str. + NO_2 angle,	C: 0.1185 N: 0.4642 O: 0.4173 IR: 0.0293
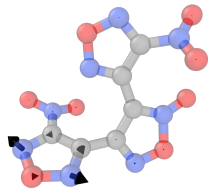 ModeID=179	902.3 915.0 928.8	906.024 916.632 925.311	Ring ONO Angle Bend, (High Press. Sens. of $\mathcal{O}$(100ps))	C: 0.2152 N: 0.6223 O: 0.1625 IR: 0.0652
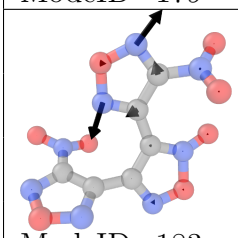 ModeID=183	908.9 917.9 930.5	910.846 927.24 939.295	In-plane ring breathing (Low Ambient $\mathcal{O}$(100ps))	C: 0.2213 N: 0.6732 O: 0.1054 IR: 0.0418
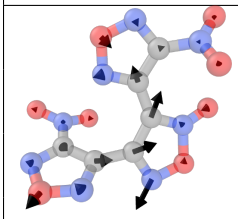 ModeID=188	951.4 965.0 979.6	960.993 970.154 977.869	C-backbone + C-C-N Angle, (Low.Press.Sens. of $\mathcal{O}$(100ps))	C: 0.3633 N: 0.3282 O: 0.3085 IR: 0.1550

Displacements	**Calc. Freq.** (cm^{-1})	**Expt. Freq.** (cm^{-1})	**Assignment**	**Character**
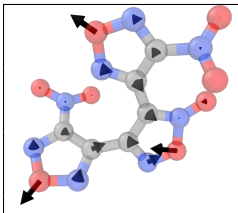 ModeID=189	1003.2 1011.8 1022.0	1001.01 1008.73 1014.52	N-O-N Angle + C-backbone	C: 0.2843 N: 0.2762 O: 0.4395 IR: 1524
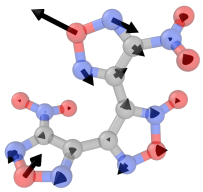 ModeID=196	1032.2 1042.6 1057.4	1037.66 1048.27 1056.95	O-N-O Angle on Ring (Low Ambient $\mathcal{O}$(100ps))	C: 0.1924 N: 0.3617 O: 0.4459 IR: 0.0632
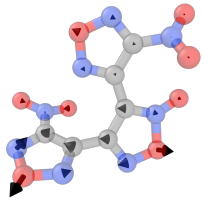 ModeID=200	1041.6 1056.1 1076.2	1042.96 1059.84 1071.90	Ring O-N-O Sym. Stretch, (High Press. Sens. & Low Amb. $\mathcal{O}$(100ps))	C: 0.2388 N: 0.3031 O: 0.4580 IR: 0.0820
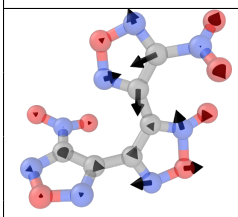 ModeID=202	1114.0 1124.6 1139.1	1120.11 1131.69 1140.85	C-C-N Angle + N-O-N Angle, (High Ambient $\mathcal{O}$(100ps))	C: 0.3371 N: 0.3423 O: 0.3205 IR: 0.0886
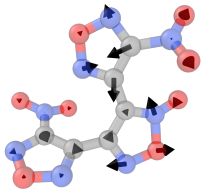 ModeID=204	1116.7 1128.8 1143.8	1126.38 1140.37 1150.49	N-C-C Angle + O-N-O Ring Angle (Low Press. Sens. of $\mathcal{O}$(100ps))	C: 0.3362 N: 0.3469 O: 0.3170 IR: 0.0184
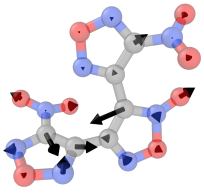 ModeID=208	1166.1 1189.3 1213.9	1176.53 1198.23 1214.62	N-C-C Angle + C-N-O Ring Angle (Low Press. Sens. of $\mathcal{O}$(100ps))	C: 0.4420 N: 0.2505 O: 0.3075 IR: 0.0871

Displacements	**Calc. Freq.** (cm^{-1})	**Expt. Freq.** (cm^{-1})	**Assignment**	**Character**
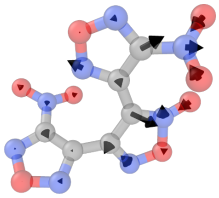 ModeID=210	1272.0 1288.7 1308.4	1285.99 1303.34 1316.84	N-O Sym. Str. + C-C-C Angle	C: 0.3639 N: 0.3393 O: 0.2969 IR: 0.1903
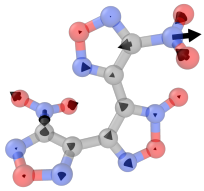 ModeID=217	1313.8 1341.3 1369.1	1318.77 1339.03 1353.97	NO Sym Stretch + CN Stretch, (High Ambient $\mathcal{O}$(100ps))	C: 0.2397 N: 0.4116 O: 0.3488 IR: 1.0581
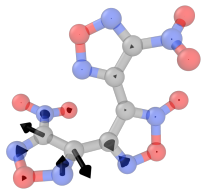 ModeID=225	1376.2 1402.4 1429.5	1355.42 1377.12 1392.07	CC Stretch + CN Stretch, (High Press. Sens. of $\mathcal{O}$(100ps))	C: 0.4970 N: 0.4013 O: 0.1017 IR: 0.0576
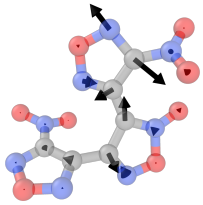 ModeID=239	1480.5 1507.9 1533.1	1448.48 1474.04 1493.32	C-N Stretch on Backbone (High Ambient $\mathcal{O}$(100ps))	C: 0.5515 N: 0.3599 O: 0.0886 IR: 0.0824
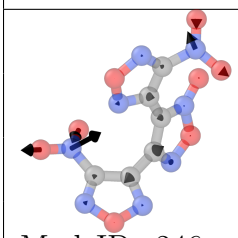 ModeID=246	1525.2 1535.2 1549.7	1523.22 1545.88 1562.76	N-O Asymmetric Stretch (amine)	C: 0.2250 N: 0.4349 O: 0.3402 IR: 1.3433
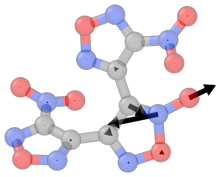 ModeID=261	1657.3 1668.0 1689.1	1642.32 1664.59 1685.72	N-O Asymmetric Stretch	C: 0.2672 N: 0.4252 O: 0.3076 IR: 1.6929

While an elegant theory for initiation and VET in molecular crystals, the phonon-up-pumping model necessitates the determination of so-called doorway modes in the vibrational spectrum. This is challenging as it implies a small subset of modes are coupled to both the phonon bath (continuous spectra below $\sim$150 cm^{-1}) and the 'fingerprint' vibrations that are characteristic of the bonding topology. Figure S3A displays the total vibrational spectrum (Raman and IR active) of BNFF where one could not unambiguously label doorway modes. We adopt the method of Michalchuk et al.,[5] where the vibrational spectra is sectioned by integer multiples of the phonon band edge (ω_{max}) frequency. This states that modes $< \omega_{max}$ are designated phonons, $\omega_{max} < \omega < 2\omega_{max}$ are the doorway modes, and any mode $> 2\omega_{max}$ is a fingerprint mode of the material. Table S3 collects these frequency intervals for each of the studied pressures.

S2.2 Two-Phonon Density of States

Data shown here utilizes the calculated anharmonic force constants of BNFF to study the multi-vibration collisions that underpin the VET process. First, the JDOS at ambient pressure with thermal occupation of modes is shown in Figure S4 highlighting the dense spectrum of possible two-phonon signals. Not all two-vibration scattering events result in a change in population of the native (normal) modes, which is seen by overlaying the one-vibration density of states with the thermal JDOS. To determine the mode-specific scattering events we perturb the population of a given mode, and calculate the difference in the JDOS relative to thermal occupation. Integrating this difference shows where the pumped mode is strongly coupled to other vibrations in the system. Moreover, we see an increase in two-vibration scattering events with increasing pressure uniformly for all pumped vibrations indicating that there is stronger anharmonic coupling among modes. Figures S5, S6 gather this data for all modes detailed in Table S2. For clarity, the ω_{max} and $2\omega_{max}$ values for each pressure are added as solid color-matched points.

While it is clear that most of the scattering events occur among fingerprint modes, the

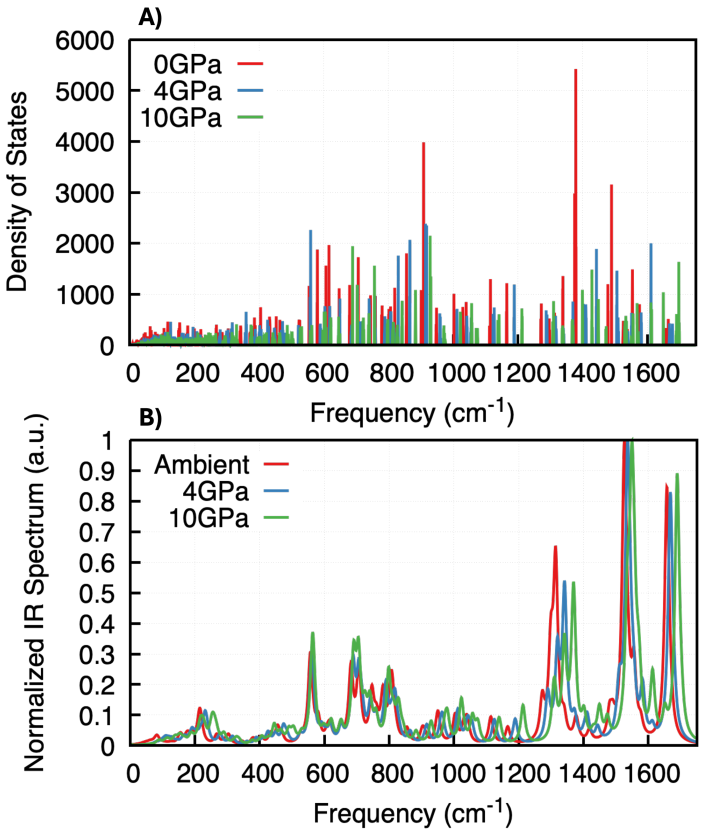

Figure S3: A) Calculated one-phonon density of states for Ambient, 4GPa, and 10GPa BNFF structures. B) Calculated IR spectra using Lorentzian lineshapes corresponding to T=300K applied to normal mode frequencies.

pressure dependent changes are most prominent in the phonon and doorway modes. To highlight this change with pressure we tally the number of scattering events in each of the integer ω_{max} windows, this data is collected in Figures S7 and S8. As a reminder, we refer to phonon modes as those $\leq \omega_{max}$ and doorway modes as $\omega_{max} < \omega < 2\omega_{max}$, dashed lines in S7 and S8 highlight these regions. The data in S7 and S8 are normalized by the number of normal modes that lie in each of the $M\omega_{max}$ to $N\omega_{max}$ regions so it is easier to compare regions with differing spectral density. All modes studied here show an increase in doorway mode scattering with pressure, highlighting the role these vibrations play in the VET process in the material. In contrast, fingerprint modes ($> 2\omega_{max}$) show no

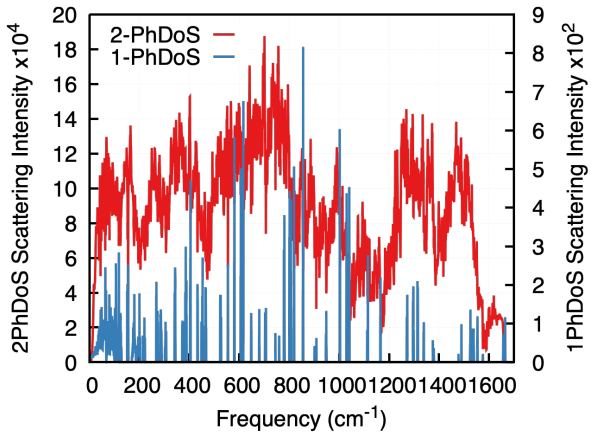

Figure S4: Calculated one- and two-phonon joint density of states for ambient pressure highlighting the dense spectrum of available two-phonon collisions. One phonon density of states is plotted on its own vertical scale for clarity.

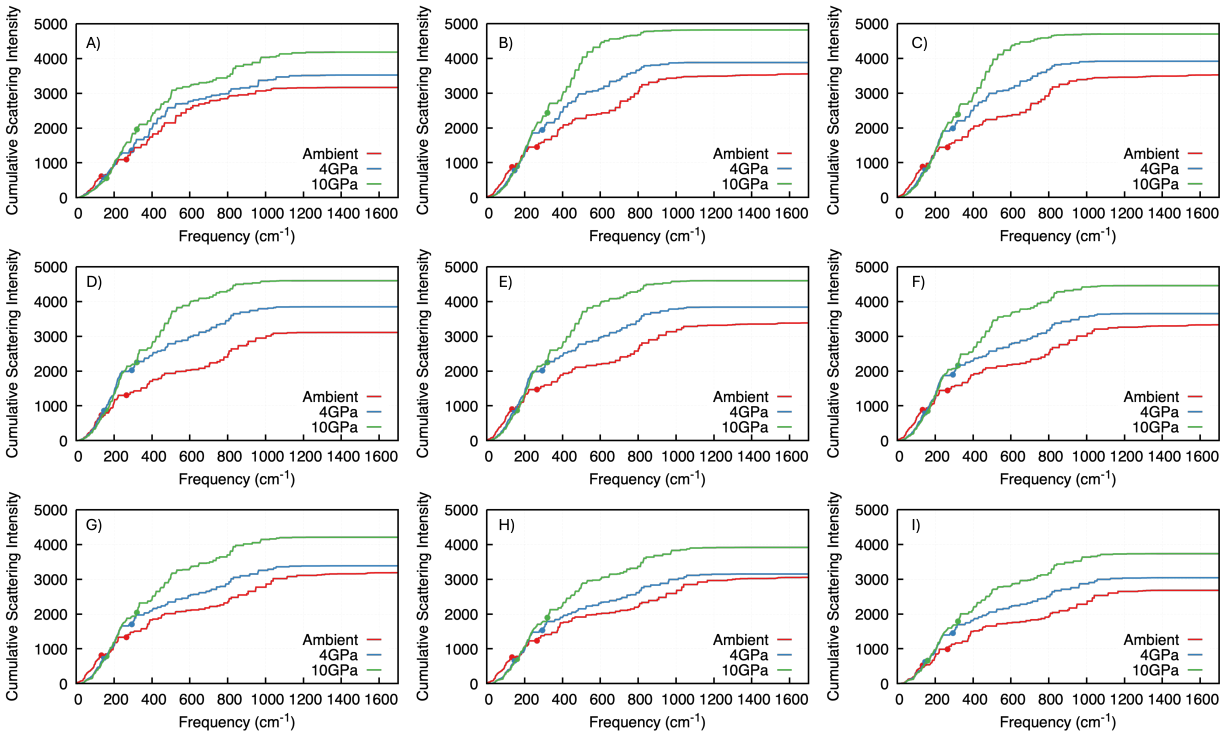

Figure S5: Integrated ΔJDOS through pressure, where circles along the curve represent the lower (w_{max}) and upper ($2w_{max}$) bounds of the doorway region for that pressure. Each panel corresponds to a pumped normal mode highlighted with more detail in Table S2. A) Normal Mode ID = 120, B) Normal Mode ID = 166, C) Normal Mode ID = 172, D) Normal Mode ID = 179, E) Normal Mode ID = 183, F) Normal Mode ID = 188, G) Normal Mode ID = 189, H) Normal Mode ID = 196, I) Normal Mode ID = 200

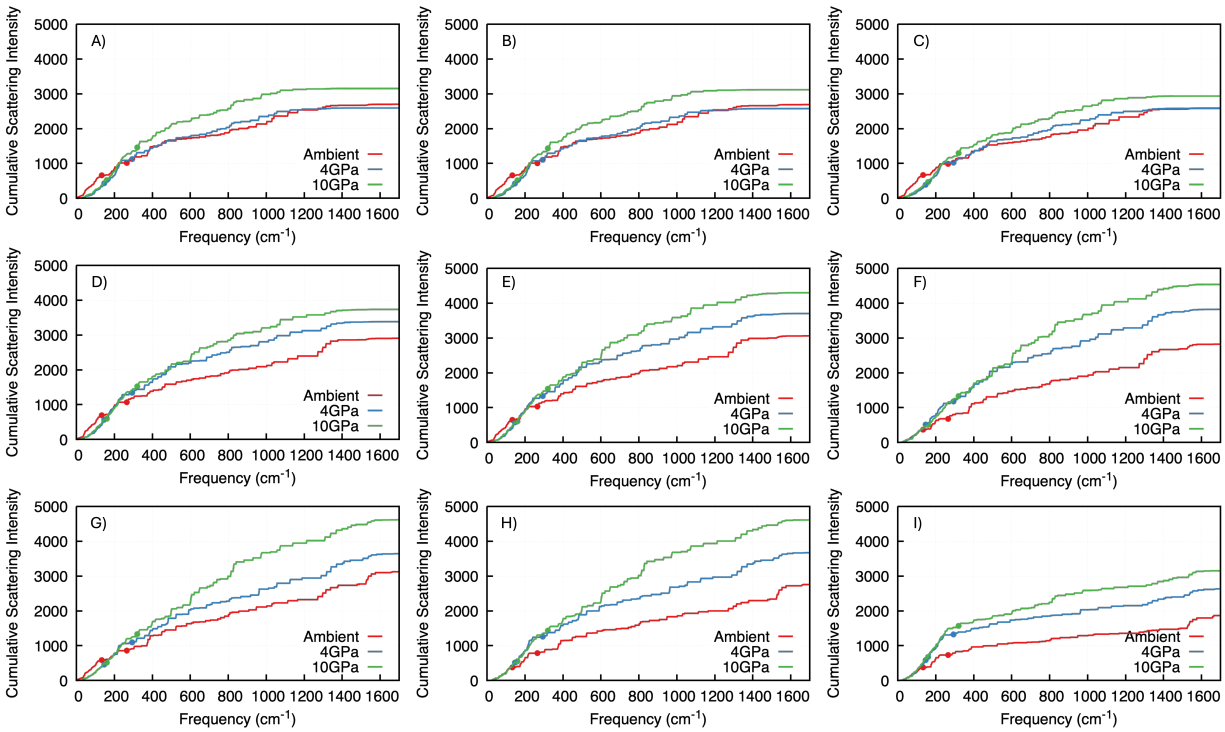

Figure S6: Integrated ΔJDOS through pressure, where circles along the curve represent the lower (w_{max}) and upper ($2w_{max}$) bounds of the doorway region for that pressure. Each panel corresponds to a normal mode highlighted with more detail in Table S2. A) Normal Mode ID = 202, B) Normal Mode ID = 204, C) Normal Mode ID = 208, D) Normal Mode ID = 210, E) Normal Mode ID = 217, F) Normal Mode ID = 225, G) Normal Mode ID = 239, H) Normal Mode ID = 246, I) Normal Mode ID = 261

clear trend of pressure sensitivity, with most showing no significant changes with increasing pressure. While we hypothesize that the $\mathcal{O}$(100ps) VET dynamics are the result of phonon modes (likely attributed to defects and surfaces) exchanging energy with fingerprint modes, the increased scattering through doorway modes does not wholly prove the experimental observation. If true, then all modes that demonstrate $\mathcal{O}$(100ps) behavior would be observed to have decreasing time constants with pressure, where we have observed a mix of pressure sensitivities. Another way of interpreting the experimental and theoretical predictions is that DFT only provides us with the *static* VET pathways, where the experiment is subject to the *dynamic* populations of coupled modes. Much like the branching reaction pathways that take energetic molecular crystals from a compressed solid to combustion products, there are emergent bottlenecks where population (chemical concentration) of coupled modes will affect the overall VET (chemical kinetics) timescales.

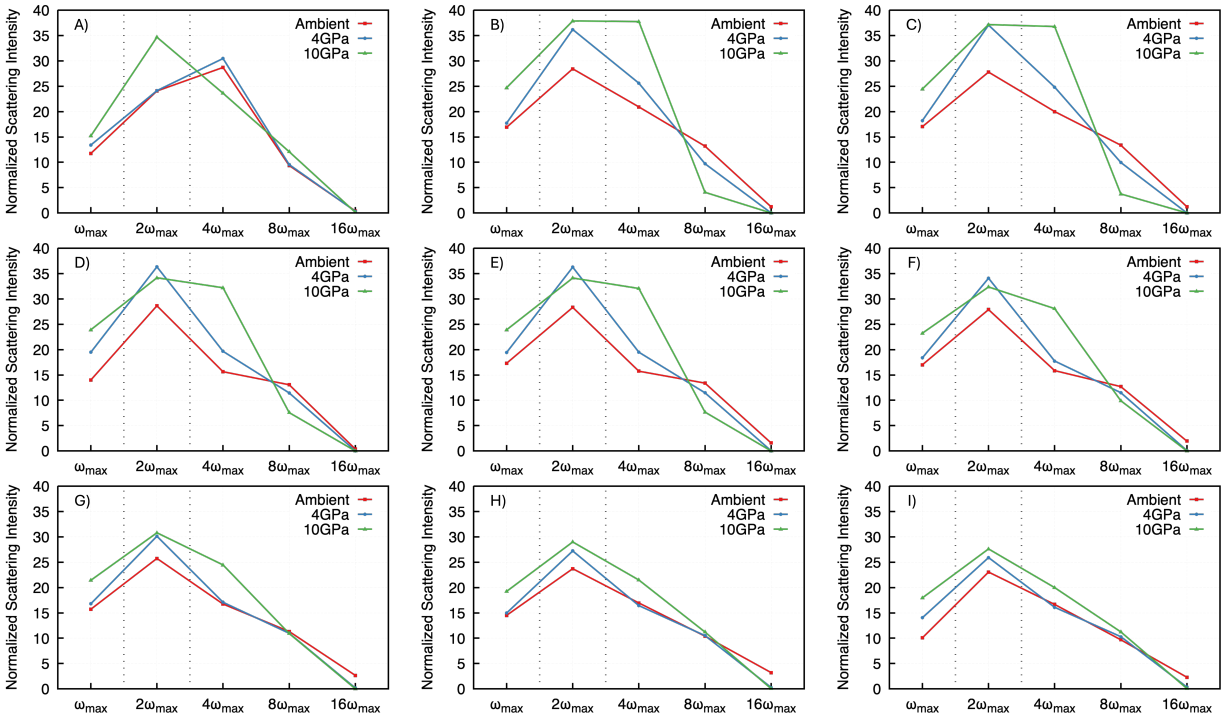

Figure S7: Normalized ΔJDOS by integrating in the spectral ranges defined by factors of ω_{max} in Table S3. Vertical axis can be read as number of scattering events per normal mode available. Vertical dashed lines show breakpoints for names given to frequency regions. Each panel corresponds to a normal mode highlighted with more detail in Table S2. A) Normal Mode ID = 120, B) Normal Mode ID = 166, C) Normal Mode ID = 172, D) Normal Mode ID = 179, E) Normal Mode ID = 183, F) Normal Mode ID = 188, G) Normal Mode ID = 189, H) Normal Mode ID = 196, I) Normal Mode ID = 200

Table S3: Designation of types of modes within BNFF for the purpose of identifying where scattering intensity changes with pressure.

	Pressure (GPa)	Frequency Range (cm^{-1})	Normal Mode Range	Normal Mode Count
Long./Trans. Phonons	0	0-132.6 (ω_{max})	1-52	52
	4	0-146.8 (ω_{max})	1-44	44
	10	0-160.2 (ω_{max})	1-37	37
Doorway Modes	0	132.6-265.2	53-72	20
	4	146.8-293.6	45-71	27
	10	160.2-320.4	37-76	40
Fingerprint Modes	0	265.2-1800	73-264	192
	4	293.6-1800	72-264	193
	10	320.4-1800	77-264	187

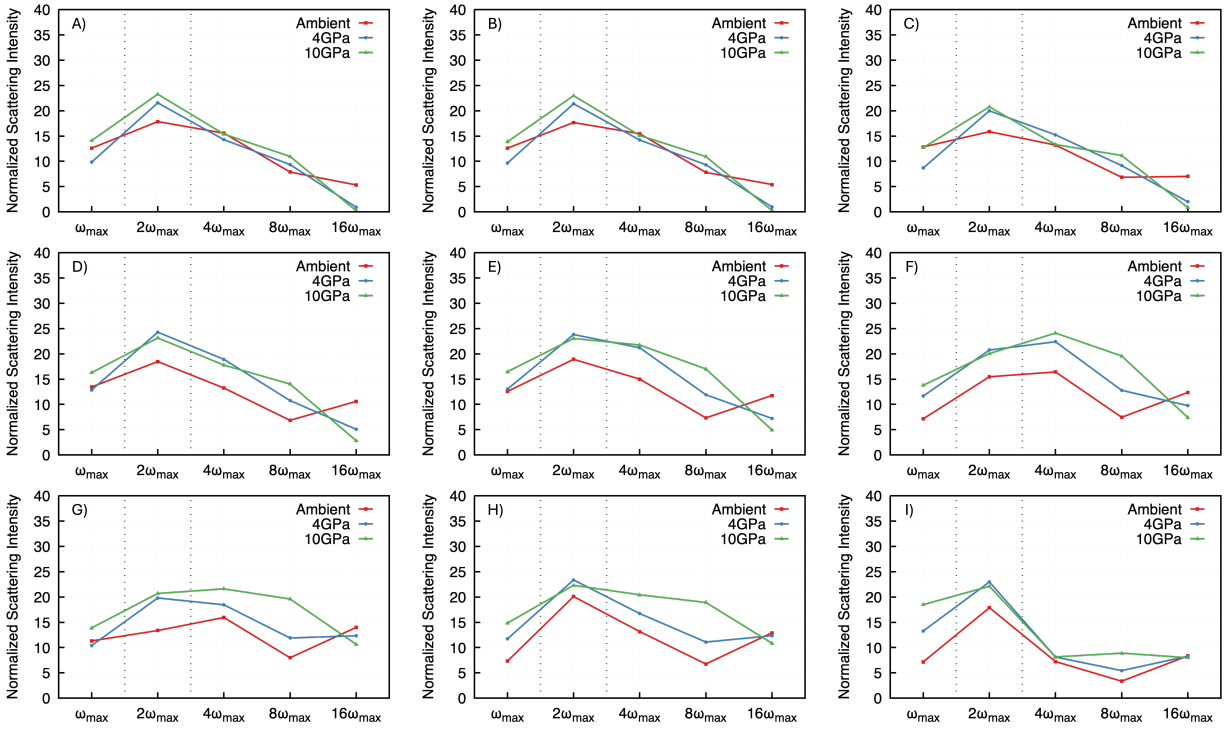

Figure S8: ΔJDOS by integrating in the spectral ranges defined by factors of ω_{max} in Table S3. Vertical axis can be read as number of scattering events per normal mode available. Vertical dashed lines show breakpoints for names given to frequency regions. Each panel corresponds to a normal mode highlighted with more detail in Table S2. A) Normal Mode ID = 202, B) Normal Mode ID = 204, C) Normal Mode ID = 208, D) Normal Mode ID = 210, E) Normal Mode ID = 217, F) Normal Mode ID = 225, G) Normal Mode ID = 239, H) Normal Mode ID = 246, I) Normal Mode ID = 261

S3 Experimental Results

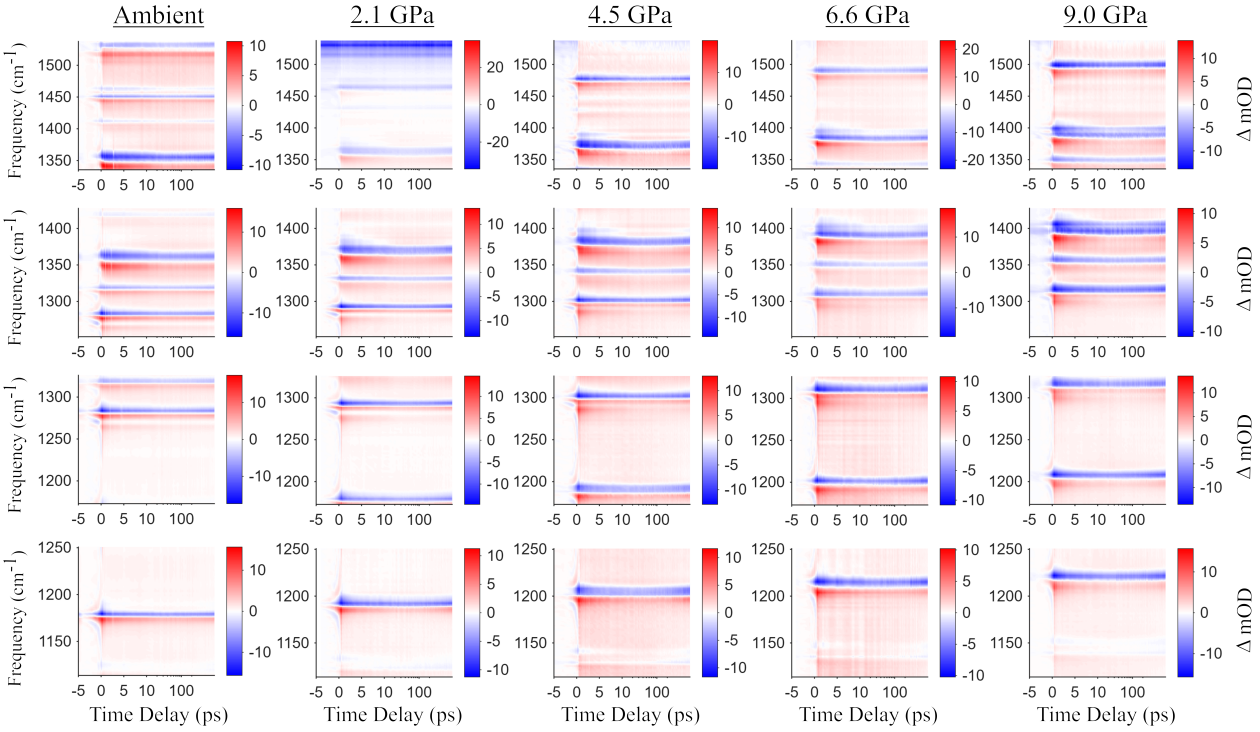

Figure S9: Transient absorption spectra of BNFF from ambient pressure to 9.0 GPa, with 1675 cm^{-1} vibrational excitation occurring at time t=0. Time delays are linear from -5 ps to 10 ps, and then logarithmic from 10 ps to 300 ps.

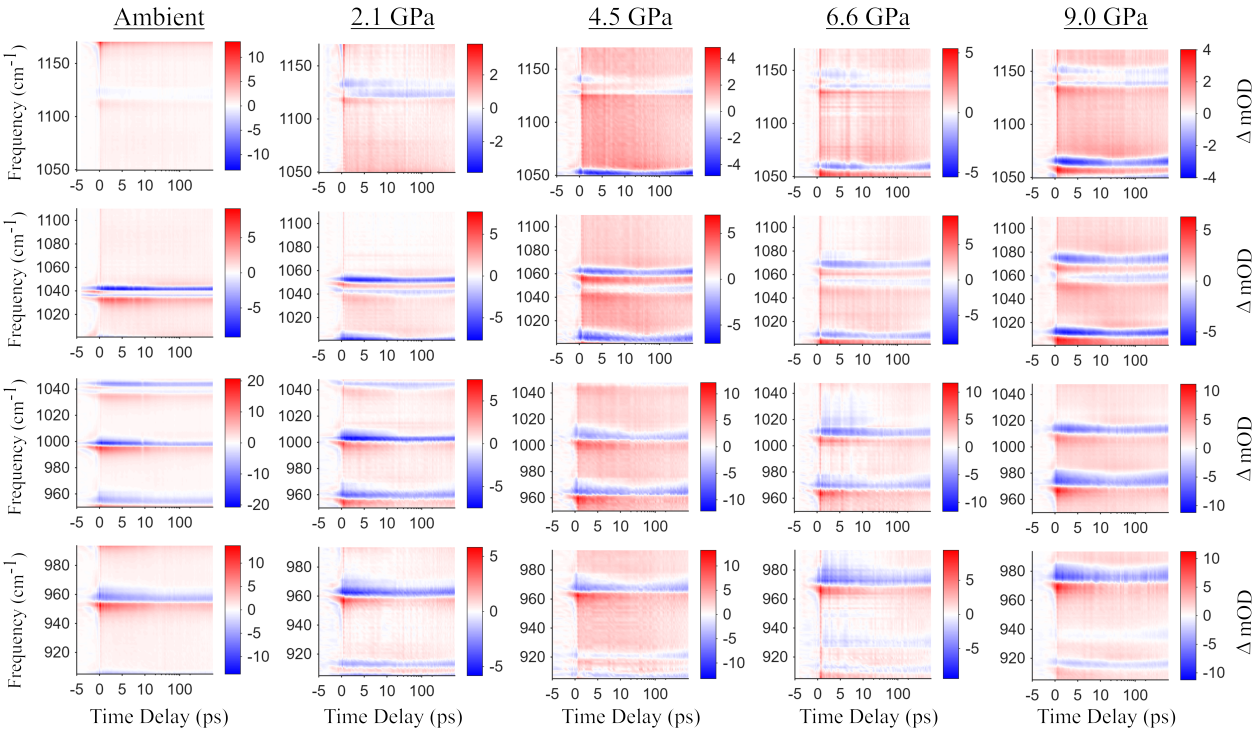

Figure S10: Transient absorption spectra of BNFF from ambient pressure to 9.0 GPa, with 1675 cm^{-1} vibrational excitation occurring at time t=0. Time delays are linear from -5 ps to 10 ps, and then logarithmic from 10 ps to 300 ps.

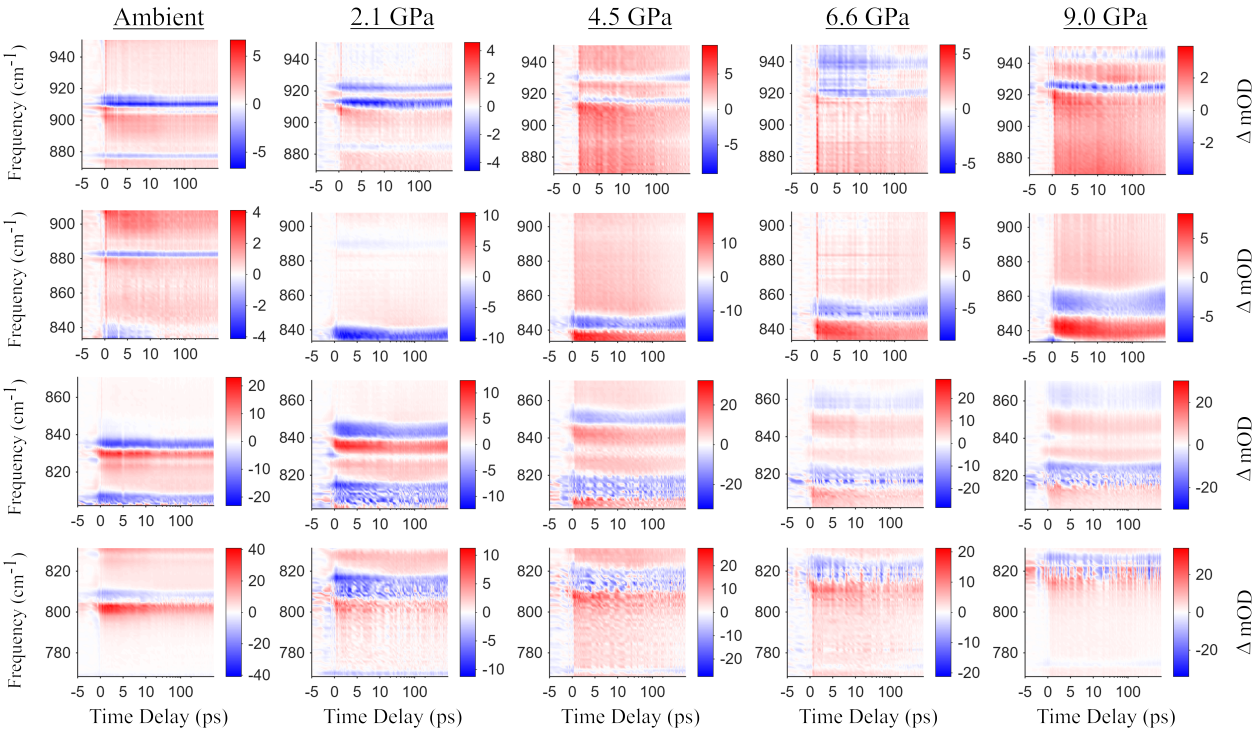

Figure S11: Transient absorption spectra of BNFF from ambient pressure to 9.0 GPa, with 1675 cm^{-1} vibrational excitation occurring at time t=0. Time delays are linear from -5 ps to 10 ps, and then logarithmic from 10 ps to 300 ps.

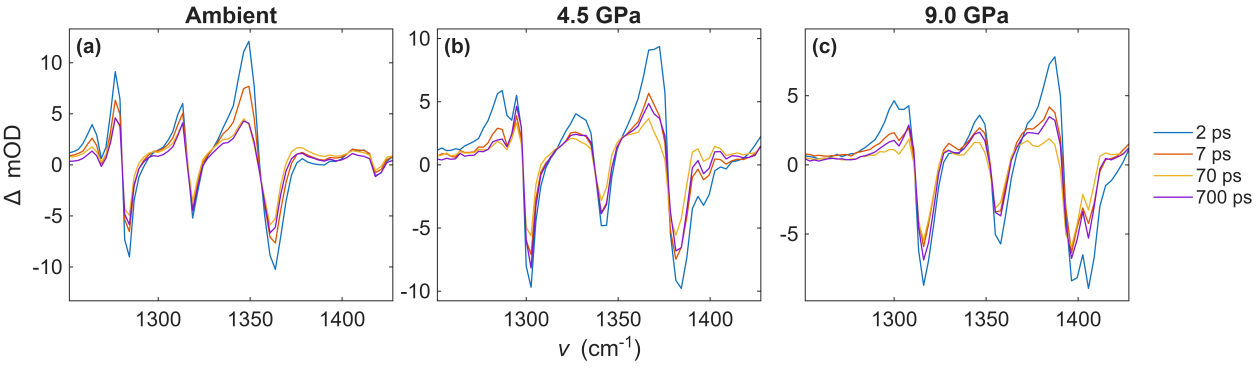

Figure S12: Example transient spectra at select time delays centered around 1350 cm^{-1} for (a) ambient pressure (b) 4.5 GPa and (c) 9.0 GPa. The induced absorption feature centered around 1348 cm^{-1} indicates no participation in the O(100 ps) dynamics at ambient pressure as the signal remains unchanged between 70 and 700 ps. However under pressure, the O(100 ps) dynamics is observed as the 700 ps signal level is higher than the 70 ps signal level.

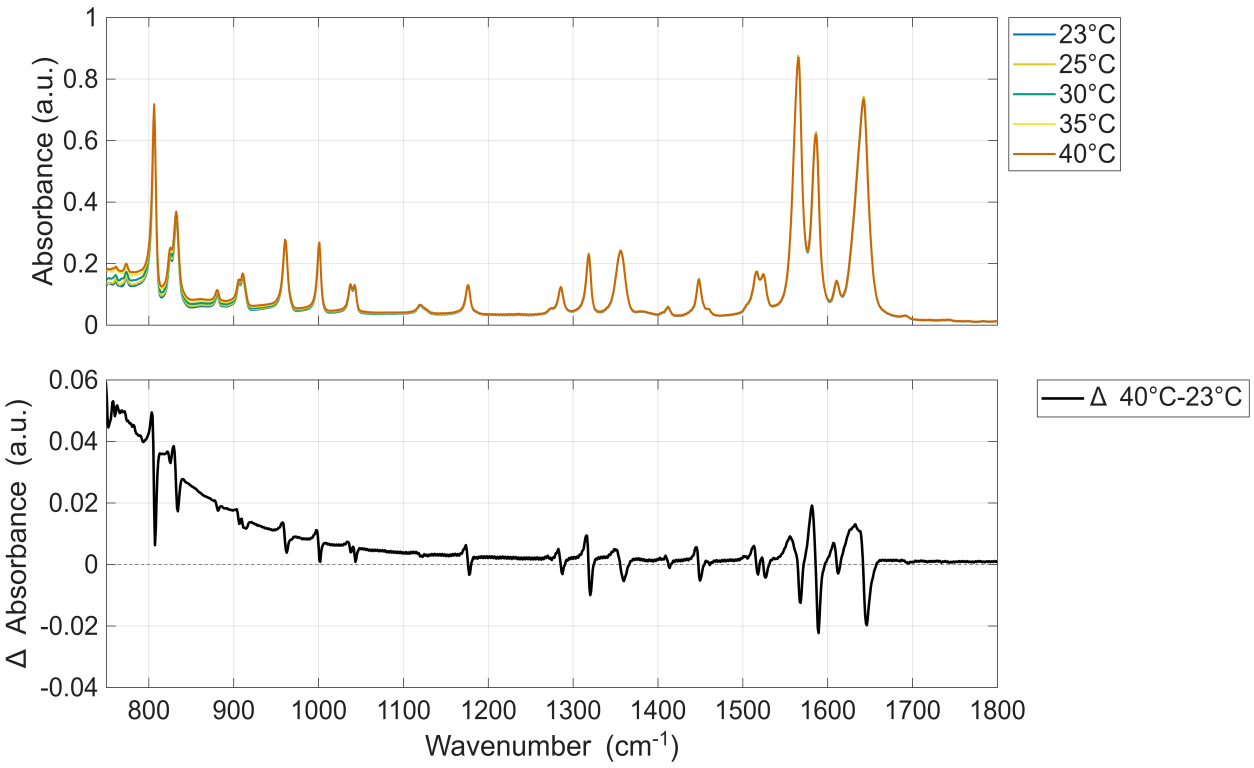

Figure S13: (Top) FTIR absorption spectra of BNFF thin films heated to 23°C, 25°C, 30°C, 35°C, and 40°C. (Bottom) Difference spectrum between 40°C and 23°C, highlighting the lineshape changes expected for high frequency vibrations due to a thermally excited phonon bath.

S4 Global Analysis of the Time-Resolved Spectra

Global target analysis of the transient spectra were performed using `glotaran-legacy`. Following prior ultrafast VET studies, a sequential kinetic scheme (A→B→C→ $\cdots$) was assumed for all models. Best-fit lifetimes are summarized in Table 1 (main text). Before fitting, each dataset was aligned to a common time zero by the leading-edge rise, and only spectra at $t \geq 0$ ps were included. No measurable probe dispersion (spectral chirp) was observed, so dispersion was fixed to zero for all datasets. The instrument response function (IRF) was modeled as a Gaussian (center fixed at $t = 0$, FWHM = 400 fs). Unlike earlier VET studies that included both an ultrafast "spike" component ($\sim$ 10 fs) and a very long "infinite" component, these data require only the latter. We therefore included a single

long-lived population with $\tau = 1 \times 10^6$ fs to capture the persistent offset at the longest delays. The absence of a near-t_0 spike is consistent with excluding spectral regions where there would be pump-probe interference effects.

Simultaneous fits to all spectral windows spanning ~ 780 to ~ 1500 cm^{-1} were performed with lifetimes shared across windows. Four lifetimes, including the long-lived offset, were sufficient to reproduce the data at ambient pressure, and the same four-component model was then applied independently at each pressure. Because this analysis assumes time-dependent populations with time-invariant difference spectra, the extracted lifetimes represent characteristic time scales rather than unique mechanistic assignments. Within the fixed sequential model used here however, these time constants remain directly comparable across pressures.

S5 Analysis of the $\mathcal{O}$(100 ps) Dynamics

A range of factors indicate that the observed $\mathcal{O}$(100 ps) vibrational dynamics are not attributable to extrinsic or instrumental effects. First, when including previous experiments from our group on PETN[6] and RDX[7] thin films, similar long-time components have now been detected across multiple optical realignments over two independent laser systems in separate laboratories, reducing the possibility of timing drift, beam pointing instabilities, or other alignment-related issues. Second, the $\mathcal{O}$(100 ps) behavior is mode-selective with several vibrational modes exhibiting no significant long-term changes, demonstrating that the effect cannot be due to global laser fluctuations or slow instrumental drifts which would uniformly affect all spectral features. Third, the long-time dynamics are reproducible across independently prepared BNFF thin films on both CaF_2 substrates and diamond anvils, as well as daily sample repositioning within the pump/probe focal plane. Since the pump and probe spot sizes ($\sim$300 μm and $\sim$220 μm, respectively) sample different regions of the film on different days, the consistent long-time behavior amidst these changes indicates that the dynamics are not localized to site-specific sample defects or microstructural inhomogeneities.

Previous ultrafast VET studies on PETN and RDX have observed that the $\mathcal{O}$(100 ps) lifetime does not appear uniformly across vibrational modes. A similar mode selectivity is observed in BNFF, where some modes express strong signal intensification on this timescale while others appear to have minimal dynamics beyond the $\mathcal{O}$(1 ps) relaxation. The addition of the DAC introduces the additional dimension of how applied static pressure modulates the observed mode-selective behavior. Here, we present two complementary analyses. Section S5.1 identifies which modes exhibit strong or weak $\mathcal{O}$(100 ps) character at ambient pressure. Section S5.2 evaluates the relative pressure sensitivity of this long time behavior across different modes. In both cases, our goal is to highlight the extremes of the distributions to identify qualitative patterns that may provide mechanistic insight.

S5.1 $\mathcal{O}$(100 ps) Mode Character at Ambient Pressure

To quantify the degree to which each mode exhibits $\mathcal{O}$(100 ps) timescale evolution, target analysis was performed on temporal lineouts centered on individual modes at ambient pressure. Each lineout was fit with both a 3-lifetime and 4-lifetime model (see section S4) using the `pyglotaran` package in Python. The relative improvement in adjusted-R^2 upon adding the $\mathcal{O}$(100 ps) lifetime was then calculated. Adjusted-R^2 was selected as the comparison metric because the variance differs across lineouts due to nonuniform oscillator strengths and nonuniform probe intensity across the spectrum. This analysis reveals a small subset of modes with distinctly high $\mathcal{O}$(100 ps) character, while most modes fall along a relatively flat continuum. Two modes appear to fit worse when the $\mathcal{O}$(100 ps) component is included, but this outcome is attributed to low adjusted-R^2 values and higher noise levels in those specific datasets. Modes which display $\mathcal{O}$(100 ps) dynamics at ambient pressure were analyzed for mode localization, normalized displacement magnitude, and axis projection as described in section S5.3, however, no clear trends were found.

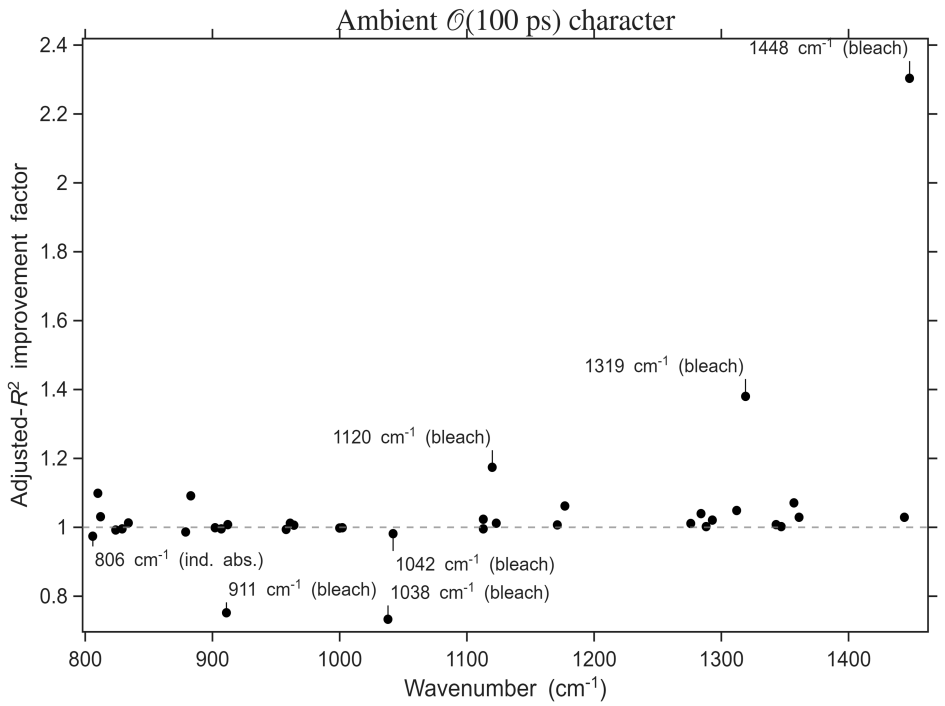

Figure S14: Adjusted-R^2 improvement factors for the addition of the $\mathcal{O}$(100 ps) lifetime in ambient-pressure fits vs wavenumber. A small subset of modes exhibit markedly high improvement, suggesting strong $\mathcal{O}$(100 ps) character, while most modes fall along a relatively flat continuum. A callout tag is added to the data points at the extreme ends of the analysis, with (bleach) indicating the lineout is centered on the ground-state bleach feature of the mode, and (ind. abs.) indicating the lineout is centered on the induced absorption feature of the mode.

S5.2 $\mathcal{O}$(100 ps) Mode-Selective Pressure Sensitivity

To evaluate the pressure sensitivity of the $\mathcal{O}$(100 ps) dynamics, temporal lineouts centered on each mode were analyzed at every pressure. For each lineout, average signal levels at 80/100/120 ps and at 820/860/900 ps were calculated and compared to capture the long-time relaxation amplitude vs pressure. To enable comparison across modes with different oscillator strengths, the signal differences at elevated pressures were normalized to the corresponding value at ambient pressure. This normalization isolates the relative change induced by applied pressure, allowing a direct comparison of pressure sensitivity across modes. As the global fit analysis implied, there is no clear pressure dependence to the overall $\mathcal{O}$(100 ps) evolution, except when comparing ambient vs. pressurized conditions.

To focus on the most physically meaningful results and extract mode-specific information, the data was subjected to two successive filtering steps: significance and consistency. First, only lineouts with a signal amplitude exceeding the corresponding 3σ noise floor were considered statistically significant. Second, for a given mode, all significant pressurized lineouts had to show a consistent sign of change (either positive or negative) relative to the ambient value to be included. After filtering, the normalized amplitudes were averaged across all the pressurized datasets for a given mode, representing "activation" due to pressure vs. the ambient case. The results are presented in Figure S15.

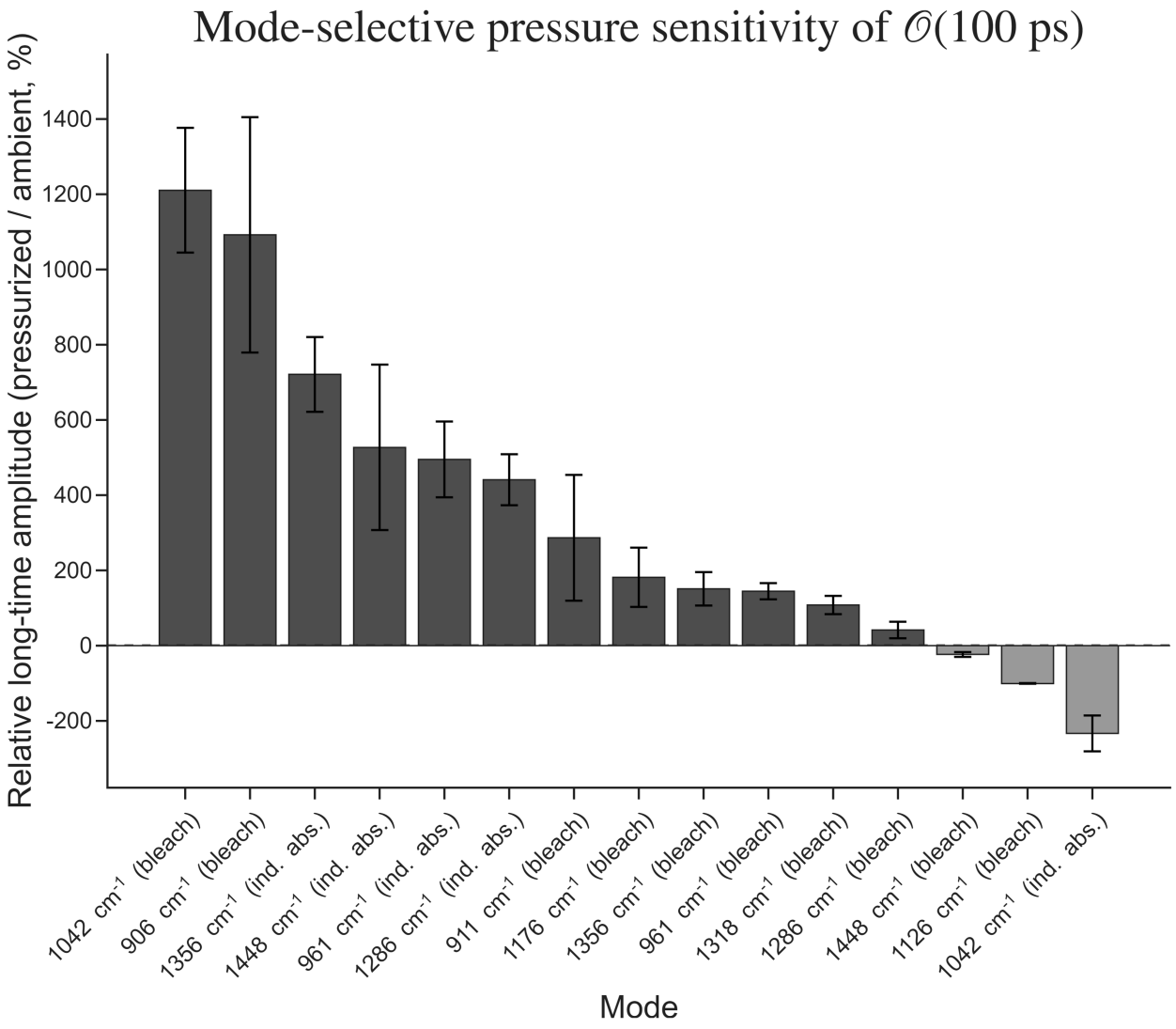

Figure S15: The change in relative long-time amplitudes for select vibrational modes by applying high static pressures. Modes are labeled by their center wavenumber at ambient pressure. Each bar represents the mean amplitude of a mode averaged over all pressurized measurements, normalized as a percentage to its ambient value. Error bars indicate the standard error of the mean. Modes are filtered for significance (pressure-induced change exceeds the 3σ noise floor) and consistency (all remaining measurements for a given mode − at least 2 − show the same sign of change, either positive or negative, relative to the ambient value), with (bleach) indicating the lineout is centered on the ground-state bleach feature of the mode, and (ind. abs.) indicating the lineout is centered on the induced absorption feature of the mode.

Interestingly, the 1042 cm^{-1} mode is present on both extremes of this analysis, where the bleach feature is the most activated under pressure and the induced absorption feature decreases the most in amplitude. This would be explained if the 1042 cm^{-1} bleach feature in-

tensifies so much that it begins to spectrally overlap with its neighboring induced absorption feature. This would indeed give a decreasing long-time amplitude for an induced absorption feature.

S5.3 Analysis of mode character in modes with high and low pressure sensitivity of $\mathcal{O}$(100 ps)

Using the optimized structures and normal mode displacements determined by density functional theory, we investigated trends for modes that exhibited both strong and weak pressure sensitivity of $\mathcal{O}$(100 ps) dynamics. The investigated metrics which demonstrated observable trends were mode localization, total mode displacement, the contributions of different chemical groups to the mode displacements, the projection of the mode displacements along the unit cell axes, and displacement weighted interatomic distances. In addition to these metrics, multiple other metrics not provided here were investigated and found to display no observable trends. The metrics which displayed no observable trends include the mode displacement projections radially from the molecular centers of mass, the center of mass displacements of the molecules, projections of mode displacements towards intermolecular neighbors, and contributions from different atomic types to the total mode displacement (i.e. C, N, or O contributions).

The modes at 906 cm^{-1}, 1043 cm^{-1}, and 1355 cm^{-1} exhibited higher pressure sensitivity and were selected for investigation. Similarly, the modes at 806 cm^{-1}, 961 cm^{-1}, and 1126 cm^{-1} exhibited low pressure sensitivity and were selected for investigation. For these modes, we take the atomic positions and the displacements from density functional theory whose calculation is described in section S1.3.

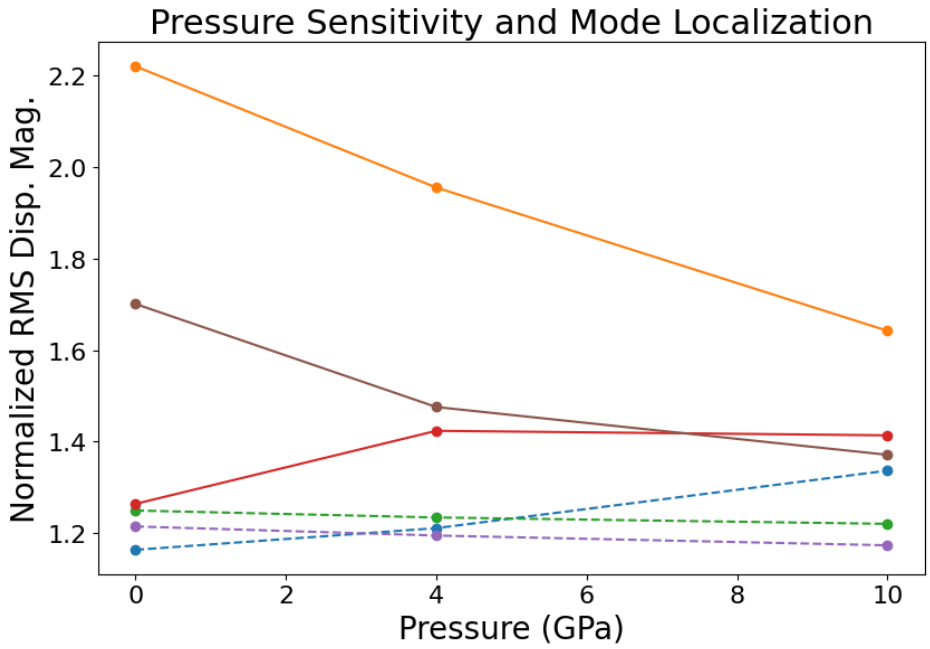

Figure S16: Normalized root mean squared displacement for pressure-insensitive modes (dashed lines) (806 cm^{-1} (blue), 961 cm^{-1} (green), 1126 cm^{-1} (purple)), and pressure-sensitive modes (solid lines) (906 cm^{-1} (orange), 1043 cm^{-1} (red), and 1355 cm^{-1} (brown)). High values indicate increased mode localization.

The mode localization was evaluated by comparing the root mean square of the atomic displacement magnitudes to the average atomic displacement magnitude divided by the square root of the atoms per units cell. In this metric, a larger value indicates a more localized mode. The results of this analysis are shown in Figure S16. The pressure sensitive modes show significantly greater localization than the pressure insensitive modes, whose displacements are spread more evenly between the atoms of the unit cell.

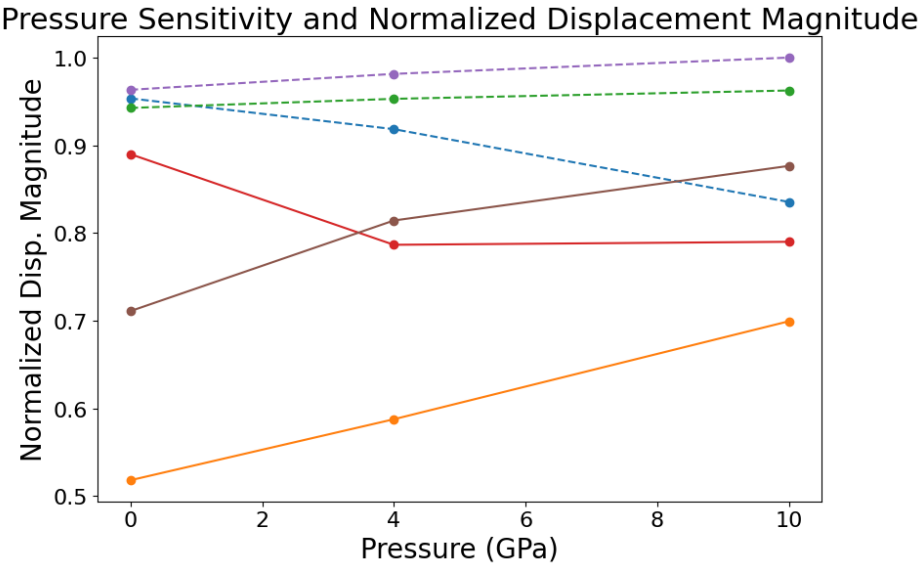

Figure S17: Total displacement magnitude for pressure-insensitive modes (dashed lines) (806 cm^{-1} (blue), 961 cm^{-1} (green), 1126 cm^{-1} (purple)), and pressure-sensitive modes (solid lines) (906 cm^{-1} (orange), 1043 cm^{-1} (red), and 1355 cm^{-1} (brown)). The displacement magnitude has been normalized to the largest displacement magnitude observed in the selected modes across all pressures.

To compare the total atomic motion between modes, we calculated the total displacement magnitude. This total displacement magnitude was determined by summing magnitudes of the atomic displacements, with the results shown in Figure S17. The pressure sensitive modes demonstrate smaller total displacements than the pressure insensitive modes.

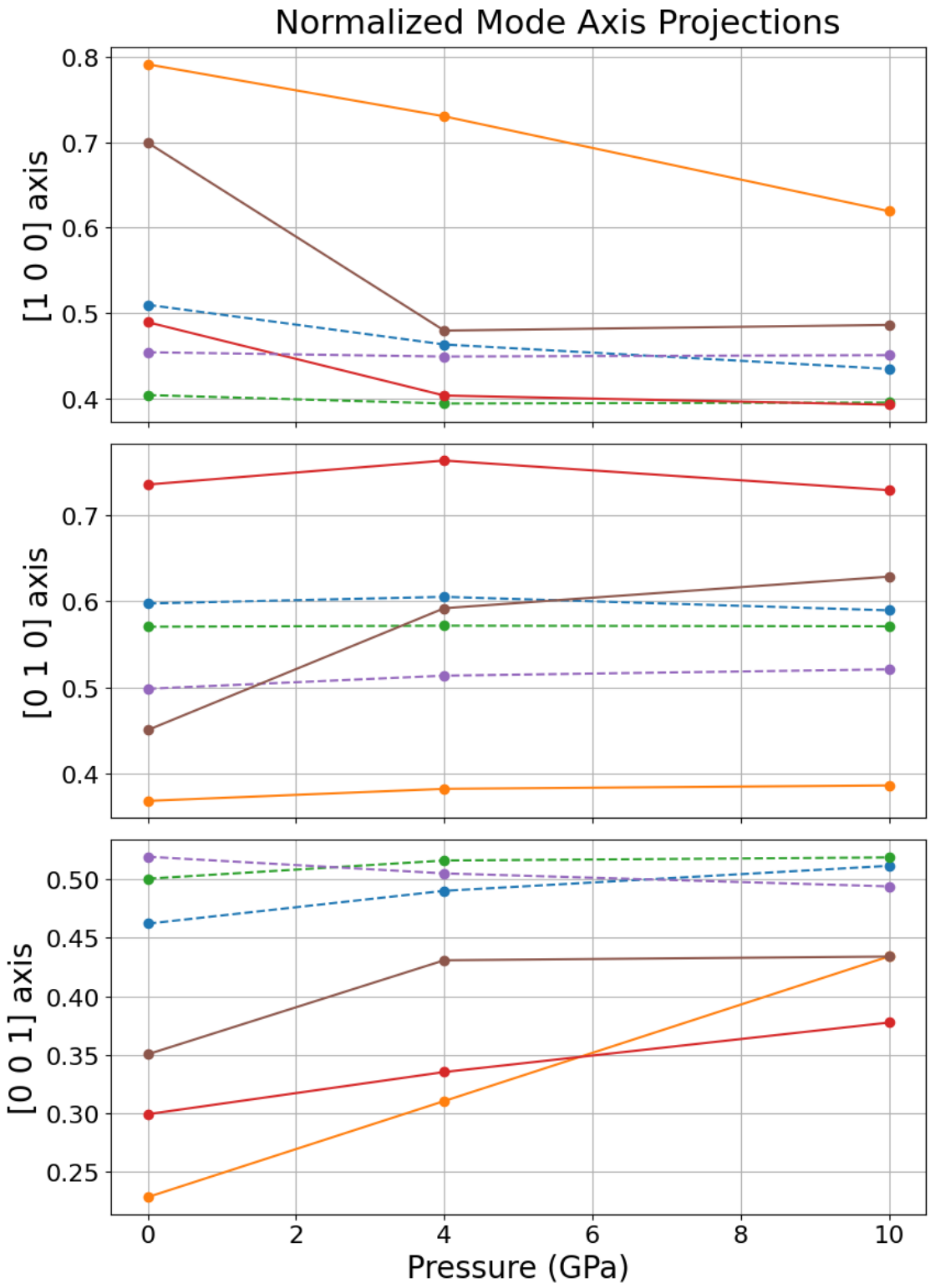

Figure S18: Projection of displacement magnitudes along the lattice parameters of the unit cell for pressure-insensitive modes (dashed lines) (806 cm^{-1} (blue), 961 cm^{-1} (green), 1126 cm^{-1} (purple)), and pressure-sensitive modes (solid lines) (906 cm^{-1} (orange), 1043 cm^{-1} (red), and 1355 cm^{-1} (brown)).

To investigate any correlations between normal mode pressure sensitivity and the compressibility of the crystal lattice, we projected the normal modes along the axes of the unit cell. The projection along the unit cell axes was evaluated by taking the sum of the projection of the atomic displacements along each unit cell axis and normalizing it by the sum of the atomic displacement magnitudes. The axis dependent projections are shown in Figure S18. The pressure sensitive modes show greater projection along the [1 0 0] axis, which is the most compressible axis. The pressure insensitive modes show comparatively smaller projections along the [1 0 0] axis, and greater projections along the [0 0 1] axis, which the DFT optimized structures indicate is ∼55% as compressible as the [1 0 0] axis. This indicates that the pressure sensitivity is in part tied to the compressibility of of the unit cell, with greater sensitivity to pressure for displacements along the most compressible axes of the unit cell.

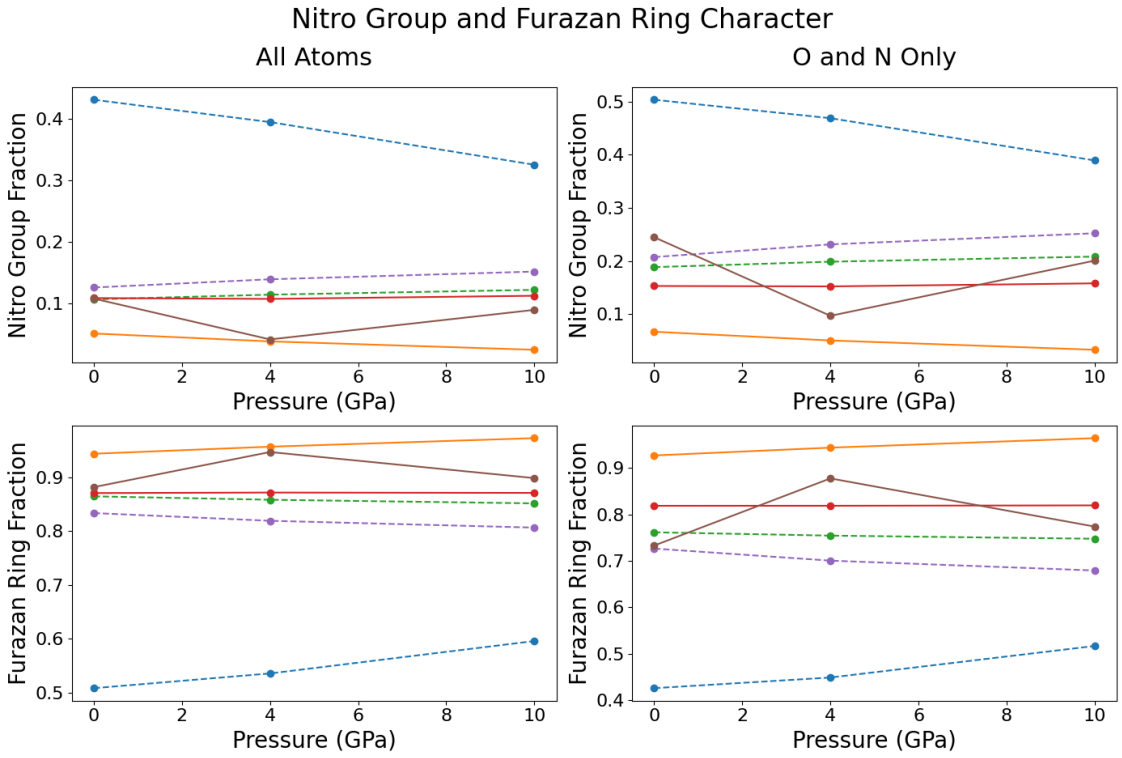

Figure S19: Fraction of normal mode displacement magnitudes in furazan rings and nitro groups for pressure-insensitive modes (dashed lines) (806 cm^{-1} (blue), 961 cm^{-1} (green), 1126 cm^{-1} (purple)), and pressure-sensitive modes (solid lines) (906 cm^{-1} (orange), 1043 cm^{-1} (red), and 1355 cm^{-1} (brown)).

We also investigated correlations between pressure sensitivity and functional group participation in the normal modes. To calculate the contribution of a chemical group to a normal mode we compute the sum of the displacement magnitudes for atoms belonging to that chemical group. This was conducted in two ways. The first approach summed over the displacement magnitudes of all atom types and was normalized by the total displacement magnitude of the normal mode. The second approach summed over only contributions from the displacement magnitudes of oxygen and nitrogen atoms to each chemical group and was normalized by the total displacement magnitude of all nitrogen and oxygen atoms in the unit cell. Pressure sensitive modes demonstrate smaller nitro group displacements and larger furazan ring deformation than pressure insensitive modes. This indicates that pressure sensitivity may be tied to ring deformation and changes in intramolecular interaction rather than intermolecular interactions.

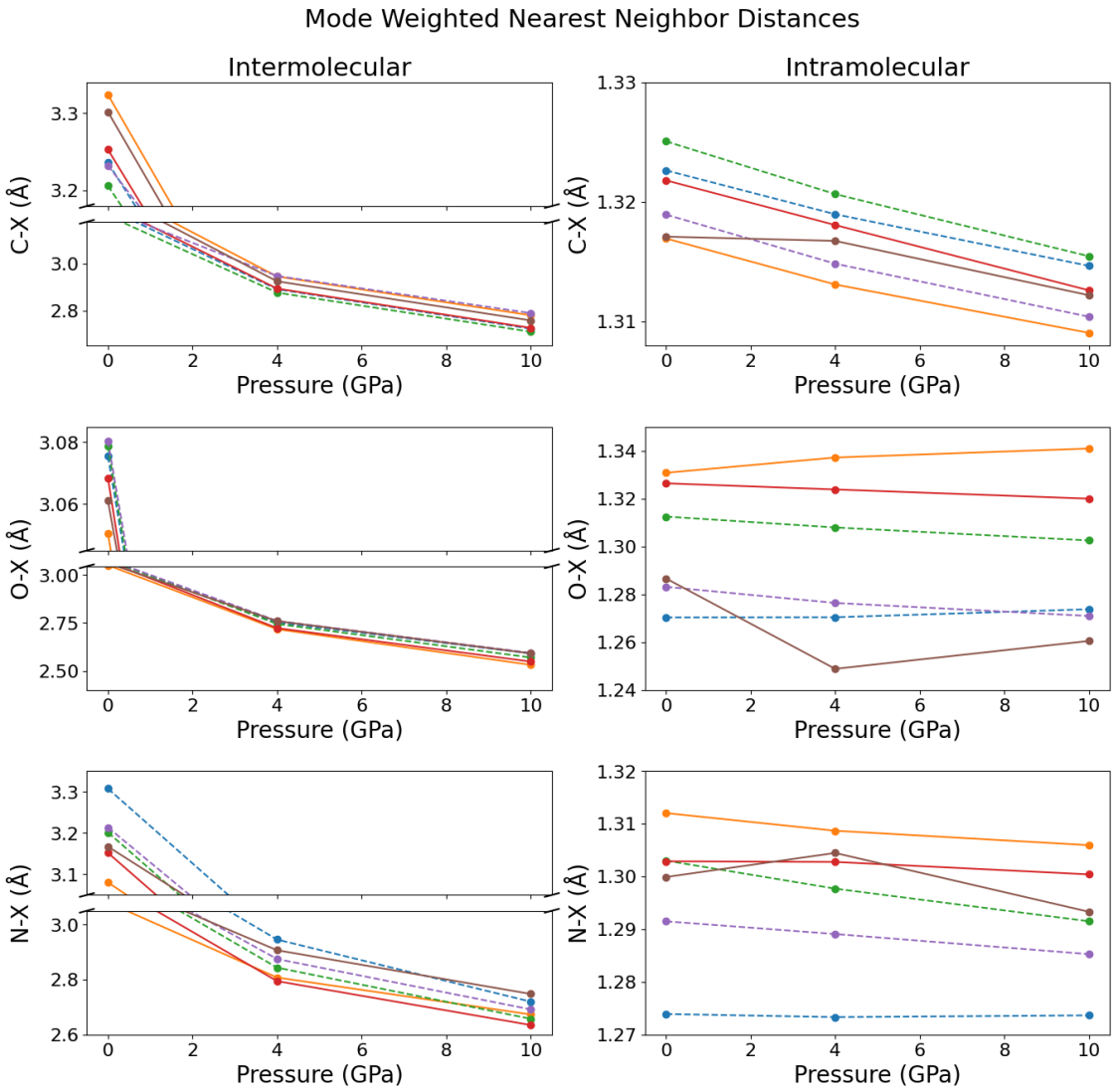

Figure S20: Nearest neighbor intermolecular and intramolecular distances weighted by normal mode displacement magnitudes for pressure-insensitive modes (dashed lines) (806 cm^{-1} (blue), 961 cm^{-1} (green), 1126 cm^{-1} (purple)), and pressure-sensitive modes (solid lines) (906 cm^{-1} (orange), 1043 cm^{-1} (red), and 1355 cm^{-1} (brown)).

The weighted average of the nearest neighbor interatomic distances was calculated using the atomic displacement magnitudes as weights. These distances were calculated from the specified atom type to its nearest neighbor of any atom type. The calculation was performed for both intermolecular and intramolecular nearest neighbor distances. The resulting average nearest neighbor distances are shown in Figure S20. Pressure sensitive modes show larger intramolecular nitrogen and oxygen nearest neighbor distances than pressure insen-

sitive modes. The pressure sensitive mode at 1355 cm^{-1}, which breaks the trend observed in other the modes, exhibits a very small total oxygen displacement with contributions for oxygen atoms accounting for only ∼15% of the total displacement magnitude of the mode. This observed trend is correlated with the greater furazan ring character observed in pressure sensitive modes, which exhibit longer bond lengths on average. For the intermolecular distances, we observed shorter average oxygen and nitrogen nearest neighbor distances for pressure sensitive modes, indicating that strong intermolecular interactions may not be a determining factor in the pressure sensitivity of the $\mathcal{O}$(100 ps) dynamics of BNFF.

The results of this displacement analysis indicate that modes with pressure-sensitive long time evolution exhibit multiple characteristics. These characteristics include small total displacement which is localized to a small number of atoms and intramolecular interactions within the furazan rings. In addition to these characteristics we observe that mode projections along the compressible crystal axis also plays a role in the determination of pressure sensitivity. These observations while not definitively conclusive indicate qualitative correlations in mode character.

S6 Mode-Specific Grüneisen Parameters

To provide a quantitative comparison of the pressure dependence of BNFF vibrational frequencies in experiment and theory, we evaluated mode-specific Grüneisen parameters using both the FTIR spectra and the DFT-calculated frequencies at 0 and 9-10 GPa. The Grüneisen parameter for mode i is defined as

$$\gamma_i = -\frac{V}{\omega_i}\frac{\partial \omega_i}{\partial V}, \tag{S2}$$

where V is the unit cell volume and ω_i is the mode frequency. For comparison with the discrete frequency–pressure data in this work, we evaluate γ_i using a finite-difference approximation between ambient and high-pressure conditions, taking the 0 and 10 GPa

DFT volumes (Table S1) and the corresponding calculated frequencies for each mode (Table S2). Experimental values γ_i^{exp} were obtained using experimental frequencies at ambient and 9 GPa and the same DFT volumes at 0 and 10 GPa as an approximation:

$$\gamma_i \approx -\frac{V_{\mathrm{avg}}}{\omega_{i,\mathrm{avg}}} \frac{\Delta\omega_i}{\Delta V}, \tag{S3}$$

where

$$V_{\mathrm{avg}} = \tfrac{1}{2}\left[V(P_1) + V(P_2)\right],$$
$$\omega_{i,\mathrm{avg}} = \tfrac{1}{2}\left[\omega_i(P_1) + \omega_i(P_2)\right],$$
$$\Delta\omega_i = \omega_i(P_2) - \omega_i(P_1),$$
$$\Delta V = V(P_2) - V(P_1).$$

Overall, the mode-specific Grüneisen parameters obtained from experiment and DFT are in good qualitative agreement (see Table S4). All modes considered exhibit positive γ_i values, consistent with stiffening of the vibrational frequencies under compression. Modes with the largest γ_i^{DFT} also tend to show larger γ_i^{exp}, indicating that the calculations reproduce the relative pressure sensitivity of different vibrations. Quantitative differences of order 0.04-0.05 in γ_i for some modes (e.g., ModeIDs 188, 217, 225) are not unexpected given the use of DFT volumes as an approximation and the limited pressure range used for finite-difference estimates. For the purposes of this work, the level of agreement is sufficient to confirm that the DFT calculations capture the static pressure sensitivity of the BNFF vibrational spectrum. We emphasize that these Grüneisen parameters characterize the static frequency-volume response of the material and are not used directly to interpret the ultrafast vibrational energy transfer dynamics.

Table S4: Mode-specific Grüneisen parameters γ_i obtained from DFT and experiment. Experimental values use experimental frequency shifts and DFT-computed volumes at 0 and 10 GPa.

ModeID	$\omega^{\text{calc}}_{ambient}$	$\omega^{\text{calc}}_{10GPa}$	γ_i^{DFT}	$\omega^{\text{exp}}_{ambient}$	$\omega^{\text{exp}}_{9GPa}$	γ_i^{exp}
120	557.1	566.0	0.0533	–	–	–
166	808.1	827.6	0.0803	806.21	820.68	0.0599
172	819.5	843.7	0.0979	825.50	834.18	0.0352
179	902.3	928.8	0.0974	906.02	925.31	0.0709
183	908.9	930.5	0.0791	910.85	939.29	0.1035
188	951.4	979.6	0.0983	960.99	977.87	0.0586
189	1003.2	1022.0	0.0625	1001.00	1014.50	0.0451
196	1032.2	1057.4	0.0812	1037.66	1056.95	0.0620
200	1041.6	1076.2	0.1100	1042.96	1071.90	0.0921
202	1114.0	1139.1	0.0750	1120.11	1140.85	0.0618
204	1116.7	1143.8	0.0807	1126.38	1150.49	0.0713
208	1166.1	1213.9	0.1352	1176.53	1214.62	0.1072
210	1272.0	1308.4	0.0950	1286.00	1316.84	0.0798
217	1313.8	1369.1	0.1388	1318.77	1353.97	0.0887
225	1376.2	1429.5	0.1279	1355.42	1392.07	0.0898
239	1480.5	1533.1	0.1175	1448.48	1493.32	0.1026
246	1525.2	1549.7	0.0536	1523.22	1562.76	0.0863
261	1657.3	1689.1	0.0640	1642.32	1685.72	0.0878

References

(1) Hack, J. H.; Lewis, N. H. C.; Knight, S.; Carpenter, W. B.; De Marco, L.; Ramasesha, K.; Tokmakoff, A. Generation and Implementation of Continuum Infrared Pulses for Broadband Detection in 2D IR Spectroscopy. *The Journal of Physical Chemistry A* **2024**, *128*, 4901–4910, Publisher: American Chemical Society.

(2) Petersen, P. B.; Tokmakoff, A. Source for ultrafast continuum infrared and terahertz radiation. *Optics Letters* **2010**, *35*, 1962–1964, Publisher: Optica Publishing Group.

(3) Cole-Filipiak, N. C.; Marquez, M.; Knepper, R.; Harmon, R.; Wiese-Smith, D.; Schrader, P.; Wood, M.; Ramasesha, K. Ultrafast spectroscopic studies of vibrational energy transfer in energetic materials. *AIP Conference Proceedings* **2020**, *2272*, 060006.

(4) Kazakov, A. I.; Dashko, D. V.; Nabatova, A. V.; Stepanov, A. I.; Lempert, D. B. Thermochemical and Energy Characteristics of DNTF and DNFF. *Combustion, Explosion, and Shock Waves* **2018**, *54*, 147–157.

(5) Michalchuk, A. A. L.; Trestman, M.; Rudić, S.; Portius, P.; Fincham, P. T.; Pulham, C. R.; Morrison, C. A. Predicting the reactivity of energetic materials: an ab initio multi-phonon approach. *Journal of Materials Chemistry A* **2019**, *7*, 19539–19553, Publisher: The Royal Society of Chemistry.

(6) Cole-Filipiak, N. C.; Knepper, R.; Wood, M.; Ramasesha, K. Sub-picosecond to Sub-nanosecond Vibrational Energy Transfer Dynamics in Pentaerythritol Tetranitrate. *The Journal of Physical Chemistry Letters* **2020**, *11*, 6664–6669, Publisher: American Chemical Society.

(7) Cole-Filipiak, N. C.; Knepper, R.; Wood, M.; Ramasesha, K. Mode-Selective Vibrational Energy Transfer Dynamics in 1,3,5-Trinitroperhydro-1,3,5-triazine (RDX) Thin Films. *The Journal of Physical Chemistry A* **2021**, *125*, 7788–7802, Publisher: American Chemical Society.